

The relation between galaxies and the warm-hot circumgalactic medium probed with X-ray and UV line absorption in the EAGLE simulation

Nastasha A. Wijers,¹[★] Joop Schaye,¹ Benjamin D. Oppenheimer^{2,3}

¹*Sterrewacht, Leiden University, Niels Bohrweg 2, 2333 CA Leiden, The Netherlands*

²*CASA, Department of Astrophysical and Planetary Sciences, University of Colorado, 389 UCB, Boulder, CO 80309, USA*

³*Harvard-Smithsonian Center for Astrophysics, 60 Garden St., Cambridge*

Accepted XXX. Received YYY; in original form ZZZ

ABSTRACT

We use the EAGLE cosmological simulation to study the distribution of baryons, and FUV (O VI), EUV (Ne VIII) and X-ray (O VII, O VIII, Ne IX, and Fe XVII) line absorbers, around low-redshift galaxies and haloes of different masses. We work with column densities, but quantify their relation with equivalent widths by analysing virtual spectra. Halo gas dominates the highest column density absorption for X-ray lines, but lower-density gas contributes to strong UV absorption lines from O VI and Ne VIII. Of the O VII (O VIII) absorbers detectable in an Athena X-IFU blind survey, we find that 41 (56) per cent arise from haloes with $M_{200c} = 10^{12.0-13.5} M_{\odot}$. We predict that the Athena X-IFU will be able to observe O VII (O VIII) covering fractions within 100 pkpc of 77 (46) per cent around $M_{\star} = 10^{10.5-11.0} M_{\odot}$ galaxies (59 (82) per cent for $M_{\star} > 10^{11.0} M_{\odot}$), comparable to the covering fractions observable for O VI and Ne VIII by current UV spectrographs. The circumgalactic medium (CGM) contains more metals than the interstellar medium across halo masses. The ions we study here trace the warm-hot, volume-filling phase of the CGM, but are biased towards gas at temperatures corresponding to the collisional ionization peak for each ion, and towards high-metallicity gas. Gas well within the virial radius is mostly collisionally ionized, but around and beyond this radius, and for O VI, photo-ionization becomes significant. Virial-temperature collisional ionization equilibrium ion fractions are a good predictor of column density trends with halo mass, but haloes contain a larger diversity of ions than this single-temperature model predicts.

Key words: galaxies: haloes – intergalactic medium – quasars: absorption lines

1 INTRODUCTION

It is well-established that galaxies are surrounded by haloes of diffuse gas: the circumgalactic medium (CGM). Observationally, this gas has been studied mainly through rest-frame UV absorption by ions tracing cool ($\sim 10^4$ K) or warm-hot ($\sim 10^{5.5}$ K) gas (e.g., Tumlinson et al. 2017, for a review). It has been found that the higher ions (mainly O VI) trace a different gas phase than the lower ions (e.g., H I), and that the CGM is therefore multi-phase. Werk et al. (2014) find that these phases and the central galaxy may add up to the cosmic baryon fraction around L_{\star} galaxies, but the budget is highly uncertain, mainly due to uncertainties about the ionization conditions of the warm phase.

Theoretically, we expect hot, gaseous haloes to develop

around $\sim L_{\star}$ and more massive galaxies ($\log_{10} M_{200c} M_{\odot}^{-1} \gtrsim 11.5-12.0$; e.g., Dekel & Birnboim 2006; Kereš et al. 2009; van de Voort et al. 2011; Correa et al. 2018). The hot gas phase ($\gtrsim 10^6$ K) mainly emits and absorbs light in X-rays. For example, high-energy ions with X-ray lines dominate the haloes of simulated L_{\star} galaxies (e.g. Oppenheimer et al. 2016; Nelson et al. 2018). In observations, it is, however, still uncertain how much mass is in this hot phase of the CGM.

Similarly, there are theoretical uncertainties regarding the hot CGM. For example, we can compare the EAGLE (Schaye et al. 2015) and IllustrisTNG (Pillepich et al. 2018) cosmological simulations. They are both calibrated to produce realistic galaxies. However, they find very different (total) gas fractions in haloes with $M_{200c} \lesssim 10^{12.5} M_{\odot}$ (Davies et al. 2020), implying that the basic central galaxy properties used for these calibrations do not constrain those of the CGM sufficiently. This means that, while difficult, ob-

[★] E-mail: wijers@strw.leidenuniv.nl

servations of the CGM hot phase are needed to constrain the models. The main differences here are driven by whether the feedback from star formation and black hole growth, which (self-)regulates the stellar and black hole properties in the central galaxy, ejects gas only from the central galaxy into the CGM (a galactic fountain), or ejects it from the CGM altogether, into the intergalactic medium (Davies et al. 2020; Mitchell et al. 2019).

There are different ways to try to find this hot gas. The Sunyaev-Zel'dovich (SZ) effect traces the line-of-sight free electron pressure, and therefore hot, ionized gas. So far, it has been used to study clusters, and connecting filaments in stacked observations, as reviewed by Mroczkowski et al. (2019). Future instruments (e.g., CMB-S4, Abazajian et al. 2016) might be able to probe smaller angular scales with the SZ-effect, and thereby smaller/lower-mass systems.

Dispersion measures from fast radio bursts (FRBs) measure the total free electron column density along the line of sight, but are insensitive to the redshift of the absorption. They therefore probe ionized gas in general, but the origin of the electrons can be difficult to determine (e.g., Prochaska & Zheng 2019). Ravi (2019) found, using an analytical halo model, that it might be possible to constrain the ionized gas content of the CGM and intergalactic medium (IGM) using FRBs. This does require host galaxies for FRBs to be found in order to determine their redshift, uncertainties about absorption local to FRB environments to be reduced, and galaxy positions along the FRB sight-line to be measured from (follow-up) surveys.

Another way to look for this hot phase is through X-ray emission. Unlike absorption or the SZ-effect, this scales with the density squared, and is therefore best suited for studying dense gas. However, if observed, it can give a more detailed image of a system than absorption along a single sight-line. Emission around giant spirals, such as the very massive ($M_\star = 3 \times 10^{11} M_\odot$) isolated spiral galaxy NGC 1961, has been detected (Anderson et al. 2016). Around lower-mass spirals, such hot haloes have proven difficult to find: Bogdán et al. (2015) stacked *Chandra* observations of eight $M_\star = 0.7\text{--}2 \times 10^{11} M_\odot$ spirals and found only upper limits on the X-ray surface brightness beyond the central galaxies. Anderson et al. (2013) stacked *ROSAT* images of a much larger set of galaxies (2165), and constrained the hot gas mass in the inner CGM.

In this work, we will focus on metal-line absorption. O VI absorption has been studied extensively using its FUV doublet at 1032, 1038 Å at low redshift. It has been the focus of a number of observing programmes with the *Hubble Space Telescope's Cosmic Origins Spectrograph* (HST-COS) (e.g., Tumlinson et al. 2011; Johnson et al. 2015, 2017). A complication with O VI is that the implications of the observations depend on whether the gas is photo-ionised or collisionally ionised. This is often uncertain from observational data (e.g., Carswell et al. 2002; Tripp et al. 2008; Werk et al. 2014, 2016), and simulations find that both are present in the CGM (e.g., Tepper-García et al. 2011; Rahmati et al. 2016; Oppenheimer et al. 2016, 2018; Roca-Fàbrega et al. 2019). The uncertainty in the ionization mechanism leads to uncertainties in which gas phase is traced, and how much mass is in it.

The hot phase of the CGM, predicted by analytical arguments (the virial temperatures of haloes) and hydrody-

namical simulations is difficult to probe in the FUV, since the hotter temperatures expected for $\sim L_\star$ galaxies' CGM imply higher-energy ions. One option, proposed by Tepper-García et al. (2013) and used by Burchett et al. (2019), is to use HST-COS to probe the CGM with Ne VIII (770, 780 Å) at higher redshifts ($z > 0.5$). These lines in the extreme ultraviolet (EUV) cannot be observed at lower redshifts, so for nearby systems a different approach is needed.

Many of the lines that might probe the CGM hot phase have their strongest absorption lines in the X-ray regime (e.g., Perna & Loeb 1998; Hellsten et al. 1998a; Chen et al. 2003; Cen & Fang 2006; Branchini et al. 2009). Some extragalactic O VII, O VIII and Ne IX X-ray line absorption has been found with current instruments, but with difficulty. Kovács et al. (2019) found O VII absorption by stacking X-ray observations centred on H I absorption systems near massive galaxies, though they targeted large-scale structure filaments rather than the CGM, while Ahoranta et al. (2019) found O VIII and Ne IX at the redshift of an O VI absorber. Bonamente et al. (2016) found likely O VIII absorption at the redshift of a broad Lyman α absorber. These tentative detections demonstrate that more certain, and possibly blind, extragalactic detections of these lines might be possible with more sensitive instruments.

The hot CGM of our own Milky Way galaxy can be observed more readily. Absorption from O VII has been found by e.g., Bregman & Lloyd-Davies (2007) and Gupta et al. (2012, also O VIII), and Hodges-Kluck et al. (2016) studied the velocities of O VII absorbers. Gatuuz & Churazov (2018) and studied Ne IX absorption alongside O VII and O VIII, focussing on the hot CGM and the ISM. The Milky Way CGM has also been probed with soft X-ray emission (e.g., Kuntz & Snowden 2000; Miller & Bregman 2015; Das et al. 2019), and studied using combinations of emission and absorption (e.g., Bregman & Lloyd-Davies 2007; Gupta et al. 2014; Miller & Bregman 2015; Gupta et al. 2017; Das et al. 2019).

Previous theoretical studies of CGM X-ray absorption include analytical modelling, which tends to focus on the Milky Way. For example, Voit (2019), used a precipitation-limited model to predict absorption by O VI–VIII, N V, and Ne VIII, and Stern et al. (2019) compared predictions of their cooling flow model to O VII and O VIII absorption around the Milky Way. Faerman et al. (2017) constructed a phenomenological CGM model, based on O VI–VIII absorption and O VII and O VIII emission in the Milky Way. Nelson et al. (2018) studied O VII and O VIII in IllustrisTNG, but focused on a wider range of halo masses: two orders of magnitude in halo mass around L_\star .

In Wijers et al. (2019) we used the EAGLE hydrodynamical simulation to predict the cosmic distribution of O VII and O VIII for blind observational surveys. We found that absorbers with column densities $N_{\text{O VII, O VIII}} \gtrsim 10^{16} \text{ cm}^{-2}$ typically have gas overdensities $\gtrsim 10^2$, and that absorbers with overdensities ~ 10 may be difficult to detect at all in planned surveys. Therefore, we expect that a large fraction of the X-ray absorbers detectable with the planned Athena X-IFU (Barret et al. 2016) survey, and proposed missions such as Arcus (Brenneman et al. 2016; Smith et al. 2016), are associated with the CGM of galaxies. Until such missions are launched, progress can be made with deep follow-up of FUV absorption lines with current X-ray instruments. The simulations can also help interpret the small

number of absorbers found with current instruments (e.g., Nicastro et al. 2018; Kovács et al. 2019; Ahoranta et al. 2019); e.g. Johnson et al. (2019) used galaxy information to re-interpret the lines found by Nicastro et al. (2018).

In this work, we will consider O VI (1032, 1038 Å FUV doublet), Ne VIII (770, 780 Å EUV doublet), O VII (He- α resonance line at 21.60 Å), O VIII (18.9671, 18.9725 Å doublet), Ne IX (13.45 Å), and Fe XVII (15.01, 15.26 Å). In collisional ionization equilibrium (CIE), the limiting ionisation case for high-density gas, these ions probe gas at temperatures $T \sim 10^{5.5} - 10^7$ K, covering the virial temperatures of $\sim L_*$ haloes to smaller galaxy clusters (see Fig. 1 and Table 1), as well as the ‘missing baryons’ temperature range in the warm-hot intergalactic medium (e.g., Cen & Ostriker 1999). We include O VI because this highly ionized UV ion has proved useful in *HST-COS* studies, and Ne VIII has been used to probe a hotter gas phase, albeit at higher redshifts. O VII, O VIII, and Ne IX are strong soft X-ray lines, probing our target gas temperature range, and have proven to be detectable in X-ray absorption. Fe XVII is expected to be a relatively strong line at higher energies (Hellsten et al. 1998b), probing the hottest temperatures in the missing baryons range (close to 10^7 K), and is therefore also included.

We will predict UV and X-ray column densities in the CGM of EAGLE galaxies, and explore the physical properties of the gas the various ions probe. We also investigate which haloes we are most likely to detect with the Athena X-IFU. In §2, we discuss the EAGLE simulations and the methods we use for post-processing them. In §3, we will discuss our results. We start with a general overview of the ions and their absorption in §3.1, then discuss what fraction of absorption systems of different column densities are due to the CGM (§3.2), what absorption profiles for galaxies of different masses look like (§3.3), the contents of haloes of different masses (§3.4) and what the underlying spherical gas and ion distributions are (§3.5). We look into radial profiles and covering fractions as a function of stellar mass in §3.6. We discuss our results in §4 and summarize then in §5.

Throughout this paper, we will use L_* for the characteristic luminosity in the present-day galaxy luminosity function ($\sim 10^{12} M_\odot$ haloes), and M_* for the stellar masses of galaxies. Except for centimetres, which are always a physical unit, we will prefix length units with ‘c’ if they are comoving and ‘p’ if they are proper/physical sizes. The results we present here are for redshift 0.1.

2 METHODS

In this section, we will discuss the cosmological simulations we use to make our predictions, how we extract column densities from them, and the galaxy and halo information we use.

2.1 EAGLE

The EAGLE simulations (‘Evolution and Assembly of GaLaxies and their Environments’; Schaye et al. 2015; Crain et al. 2015; McAlpine et al. 2016). These are cosmological, hydrodynamical simulations. Gravitational forces are calculated with the GADGET-3 Tree-PM scheme (Springel 2005) and hydrodynamics is im-

plemented using a smoothed particle hydrodynamics (SPH) method known as ANARCHY (Schaye et al. 2015, appendix A; Schaller et al. 2015). EAGLE uses a Λ CDM cosmogony with the Planck Collaboration et al. (2014) cosmological parameters: $(\Omega_m, \Omega_\Lambda, \Omega_b, h, \sigma_8, n_s, Y) = (0.307, 0.693, 0.04825, 0.6777, 0.8288, 0.9611, 0.248)$, which we also adopt in this work.

Here, we use the 100^3 cMpc^3 EAGLE simulation, though we made some comparisons to both smaller-volume and higher-resolution simulations to check convergence. It has a dark matter particle mass of $9.70 \times 10^6 M_\odot$, an initial gas particle mass of $1.81 \times 10^6 M_\odot$, and a Plummer-equivalent gravitational softening length of 0.70 kpc at the low redshifts we study here.

The resolved effects of a number of unresolved processes (‘subgrid physics’) are modelled in order to study galaxy formation. This includes star formation, black hole growth, and the feedback those cause, as well as radiative cooling and heating of the gas, including metal line cooling (Wiersma et al. 2009a). To prevent artificial fragmentation of cool, dense gas, a pressure floor is implemented at ISM densities.

In EAGLE, stars form in dense gas, with a pressure-dependent star formation rate designed to reproduce the Kennicutt-Schmidt relation. They return metals to surrounding gas based on the yield tables of Wiersma et al. (2009b) and provide feedback from supernova explosions by stochastically heating gas to $10^{7.5}$ K, with a probability set by the expected energy produced by supernovae from those stars (Dalla Vecchia & Schaye 2012). Black holes are seeded in low-mass haloes and grow by accreting nearby gas (Rosas-Guevara et al. 2015). They provide feedback by stochastic heating as well (Booth & Schaye 2009), but to $10^{8.5}$ K. This stochastic heating is used to prevent overcooling due to the limited resolution: if the expected energy injection from single supernova explosions is injected into surrounding dense $\sim 10^6 M_\odot$ gas particles at each time step, the temperature change is small, cooling times remain short, and the energy is radiated away before it can do any work. This means self-regulation of star formation in galaxies fails, and galaxies become too massive. The star formation and stellar and black hole feedback are calibrated to reproduce the $z = 0.1$ galaxy luminosity function, the black-hole-mass-stellar-mass relation, and reasonable galaxy sizes (Crain et al. 2015).

2.2 Column densities

We calculate column densities in the same way as in Wijers et al. (2019). In short, we use the ion fraction tables we will describe in §3.1, which we linearly interpolate in redshift, log density, and log temperature to get each SPH particle’s ion fraction. We multiply this by the tracked element abundance and mass of each SPH particle to calculate the number of ions in each particle.

We then make a 2-dimensional column density map from this ion distribution. Given an axis to project along and a region of the simulation volume to project, we calculate the number of ions in long, thin columns parallel to the projection axis. We then divide by the area of the columns perpendicular to the projection axis to get the column density in each pixel of a 2-dimensional map. In order to divide the ions in each SPH particle over the columns, we need to assume a spatial ion distribution for each particle. For this,

we use the same C2-kernel used for the hydrodynamics in the EAGLE simulations (Wendland 1995), although we only input the 2-dimensional distance to each pixel centre.

A simple statistic that can be obtained from these maps is the column density distribution function (CDDF). This is a probability density function for absorption system column density, normalized to the comoving volume probed along a line of sight. The CDDF is defined by

$$f(N, z) = \frac{\partial^2 n}{\partial \log_{10} N \partial X}, \quad (1)$$

where N is the column density, n the number of absorbers, z the redshift, and X the absorption length given by

$$dX = (1 + z)^2 (H(0) / H(z)) dz, \quad (2)$$

where $H(z)$ is the Hubble parameter.

In practice, we make column density maps along the Z -axis of the simulation box, which is a random direction for haloes. We use 32000^2 pixels of size 3.125^2 ckpc² for the column density maps, and 16 slices along the line of sight, which means the slices are 6.25 cMpc thick.

Wijers et al. (2019) found that this produces converged results for O VII and O VIII CDDFs up to column densities $N \approx 10^{16.5} \text{ cm}^{-2}$. Here we mean converged with respect to pixel size, simulation size, and simulation resolution. By default, we set the temperature of star-forming gas to be 10^4 K , since the equation of state for this high-density gas does not reflect the temperatures we expect from the ISM. However, this has negligible impacts on the column densities of O VII and O VIII. Note that all our results do neglect a hot ISM phase, which is not modelled in EAGLE, but may affect column densities in observations for very small impact parameters.

Rahmati et al. (2016) used EAGLE to study UV ion CDDFs and tested convergences for O VI and Ne VIII. They used the same slice thickness at low redshift, but a lower map resolution: 10000^2 pixels. At that resolution, they find O VI CDDFs are converged to $N \approx 10^{15} \text{ cm}^{-2}$, and Ne VIII to $N \approx 10^{14.5} \text{ cm}^{-2}$. The volume and resolution of the simulation do affect CDDFs down to lower column densities. For O VI, resolution has effects down to $N \approx 10^{14} \text{ cm}^{-2}$.

We checked the convergence of Ne IX and Fe XVII CDDFs with slice thickness, pixel size, box size, and box resolution in the same way as Wijers et al. (2019). We found that Ne IX column densities are converged up to $N \approx 10^{16} \text{ cm}^{-2}$, with $\lesssim 20$ per cent changes in the CDDF at $N \gtrsim 10^{12} \text{ cm}^{-2}$ due to factor 2 changes in slice thickness. For Fe XVII, CDDFs are converged to $N \approx 10^{15.4} \text{ cm}^{-2}$, with mostly smaller dependences on slice thickness than the other X-ray ions. (We will later see that this ion tends to be more concentrated within haloes, so on smaller scales, than the others we investigate.) The trends of effect size with column density, and the relative effect sizes of changing pixel size, slice thickness, simulation volume, and simulation resolution on the CDDFs, are similar to those for O VII and O VIII. We note that the resolution test for Fe XVII may not be reliable, since at larger column densities, this ion is largely found in high-mass haloes which are very rare or entirely absent in the smaller volume (25^3 cMpc^3) used for this test.

2.3 Galaxies and haloes

We use galaxy and halo information from EAGLE in two ways. First, we look at the properties of gas around haloes. We obtain absorption profiles (column densities as a function of impact parameter), as well as spherically-averaged gas properties as a function of (3D) distance to the central galaxy. Second, we investigate what fraction of absorption in a random line of sight with a particular column density is, on average, due to haloes (of different masses), to help interpret what might be found in a blind survey for line absorption.

We use the EAGLE galaxy and halo catalogues, which were publicly released as documented by McAlpine et al. (2016). The haloes are identified using the Friends-of-Friends (FoF) method (Davis et al. 1985), which connects dark matter particles that are close together (within 0.2 times the mean inter-particle separation, in this case), forming haloes defined roughly by a constant outer density. Other simulation particles (gas, stars, and black holes) are linked to a FoF halo if their closest dark matter particle is. Within these haloes, galaxies are then identified as subhaloes recovered by SUBFIND (Springel et al. 2001; Dolag et al. 2009), which identifies self-bound overdense regions within the FoF haloes. The central galaxy is the subhalo containing the particle with the lowest gravitational potential.

Though SUBFIND and the FoF halo finder are used to identify structures, we do not characterise haloes using their masses directly. Instead, we use M_{200c} , for halo masses, which is calculated by growing a sphere around the FoF halo potential minimum (central galaxy) until the enclosed density is the target $200\rho_c$, where $\rho_c = 3H(z)^2 (8\pi G)^{-1}$ is the critical density, and $H(z)$ is the Hubble factor at redshift z . For stellar masses, we use the stellar mass enclosed in a sphere with a 30 pkpc radius around each galaxy's lowest-gravitational-potential particle. We use centres of mass for the positions of galaxies, and the centre of mass of the central galaxy for the halo position.

Since the temperature of the gas is important in determining its ionization state, we also want an estimate of the temperature of gas in haloes of different masses. For this, we use the virial temperature

$$T_{200c} = \frac{\mu m_H}{3k} G M_{200c}^{2/3} (200\rho_c)^{1/3}, \quad (3)$$

where m_H is the hydrogen mass, G Newton's constant, and k the Boltzmann constant. We use a mean molecular weight $\mu = 0.59$, which is appropriate for primordial gas, with both hydrogen and helium fully ionized.

We extract absorption profiles around galaxies from the 2-dimensional maps described in Sec. 2.2. We extract profiles from both full maps and from maps created using only gas in haloes in particular mass ranges. Given the positions of the galaxies, we obtain radial profiles by extracting column densities and distances from pixel centres to galaxy centres, then binning column densities by distance.

We use only 2-dimensional distances (impact parameters) here, but only use the column density map for the Z -coordinate range that includes the galaxy centre. We compared this method to two variations for obtaining radial profiles (not shown): adding up column densities from the two slices closest to the halo centre, and using only galaxies at least R_{200c} away from slice edges for radial profiles. We found that this made little difference for the me-

dian column densities: profiles excluding haloes close to slice edges were indistinguishable from those using all haloes, in part because the excluded haloes were only a small part of the sample. The exceptions were the most massive haloes ($M_{200c} > 10^{13.5} M_{\odot}$), where larger haloes and small sample sizes mean the effect on the sample is larger. Even there, differences remained $\lesssim 0.2$ dex. Using two slices instead of one made a significant difference only where both predicted median column densities were well below observable limits we consider, and well below the highest halo column densities we find.

To obtain the contributions of different haloes to the CDDF, we use two approaches. In the first, which we use in the main paper, we make CDDFs by counting ions in long, thin, columns as for the total CDDFs, but we only use particles that are part of a halo’s FoF group, or inside its R_{200c} sphere. Alternatively, we make maps describing which pixels in the full column density maps belong to which haloes, if any, by checking if a pixel is within R_{200c} of a halo (in projected distance r_{\perp}). To do this, we make 2d maps of the same regions, and at the same resolution, as the column density maps. These are simple True/False maps, and we make them for every set of haloes we consider. However, the map does not include any pixel that is closer, in units of R_{200c} , to a halo from a different mass-defined set. We compare these methods for splitting up the CDDFs in Appendix B. Typically, the results are similar for larger column densities, but the FoF/ R_{200c} -only CDDFs (first method) contain more small column density values, coming largely from sightlines probing only short paths through the edges of the haloes.

The advantage of using the all-gas maps (second method) is that it is more comparable to observations, where large-scale structure around haloes will also be present. (Note, however, that we neglect peculiar velocities.) For the CDDFs, it also allows us to attribute specific pixels in the maps to a halo or the IGM, meaning we can truly split up the CDDF into different contributions. A downside is that some haloes will be close to an edge of the projected slice, meaning that absorption due to a halo in one slice will be missed, while that of another is underestimated. However, the fraction of such haloes is small (Table 4). On the other hand, absorption may also be attributed to haloes that just happen to be close (in projection) to the absorber. This is mainly an issue for lower-mass haloes. We also explore this effect Appendix B.

3 RESULTS

We start by investigating some of the simplest data on our ions: what temperatures and densities they exist at, the overall column density distribution for the ions, and how the column densities relate to equivalent widths (EWs) (§3.1). We will then investigate the contributions of different haloes to the ion CDDFs (§3.2), radial absorption profiles around galaxies (§3.3), the overall contents of haloes (§3.4) and the 3D ion distribution around galaxies (§3.5). Finally, we make some predictions that should be comparable to observations, once those become available (§3.6). These results are for $z = 0.1$. In appendix C, we compare some results to those for $z = 0.5$.

Table 1. Data for the ions we study. E_{ion} is the energy needed to remove the least bound electron from each ion, and T_{CIE} is the preferred CIE temperature of the ions. The CIE ranges are the upper and lower temperatures at which the ion fraction is 10 per cent of the CIE maximum. Ionization energies are from [Lide \(2003\)](#).

ion	E_{ion} eV	T_{CIE} $\log_{10} \text{ K}$
O VI	138.12	5.3–5.8
Ne VIII	239.10	5.6–6.1
O VII	739.29	5.4–6.5
O VIII	871.41	6.1–6.8
Ne IX	1195.83	5.7–6.8
Fe XVII	1266	6.3–7.0

Table 2. Atomic data for the absorption lines we study. For each ion, we record the wavelengths λ , oscillator strengths f_{osc} , and transition probabilities A we used to calculate the equivalent widths in Fig. 3. For resolved doublets, we only use the stronger line. The last column indicates the source of the line data: M03 for [Morton \(2003\)](#), V96 for [Verner et al. \(1996\)](#), and K18 for [Kaastra \(2018\)](#).

ion	λ Å	f_{osc}	A s^{-1}	source
O VI	1031.9261	0.1325	4.17×10^8	M03
Ne VIII	770.409	0.103	5.79×10^8	V96
O VII	21.6019	0.696	3.32×10^{12}	V96/K18
O VIII	18.9671	0.277	2.57×10^{12}	V96
	18.9725	0.139	2.58×10^{12}	V96
Ne IX	13.4471	0.724	8.90×10^{12}	V96/K18
Fe XVII	15.0140	2.72	2.70×10^{13}	K18

3.1 Column densities and equivalent widths

We begin with an overview of the ions we will consider in this work. Table 1 and Fig. 1 show the energies and temperatures associated with each ion. Fig. 1 visualizes the ionization tables we use throughout the paper. These are the tables of [Bertone et al. \(2010a,b\)](#). They tabulate the fraction of different elements in different ionization states, as a function of density, temperature, and redshift. The density- and redshift-dependence comes from the assumed uniform, but redshift-dependent [Haardt & Madau \(2001\)](#) UV/X-ray background. The tables were generated using using CLOUDY ([Ferland et al. 1998](#)), version c07.02.00. This is consistent with the radiative cooling and heating used in the EAGLE simulations ([Wiersma et al. 2009a](#)).

Using these tables, we generated the CDDFs for the ions we consider in this work, shown in Fig. 2. The ions all show distributions with roughly two regimes, with a shallow and steep slope at low and high column densities, respectively. The coloured ticks on the x-axis indicate the ‘knees’ which mark the transition between these regimes, determined visually. The ticks are for reference in other figures.

Next, we look into what rest-frame EWs different column densities typically correspond to for these ions. Though we will work with column densities in the rest of this paper, this should give a sense of what EWs those correspond to. Fig. 3 shows typical EW as a function of column density.

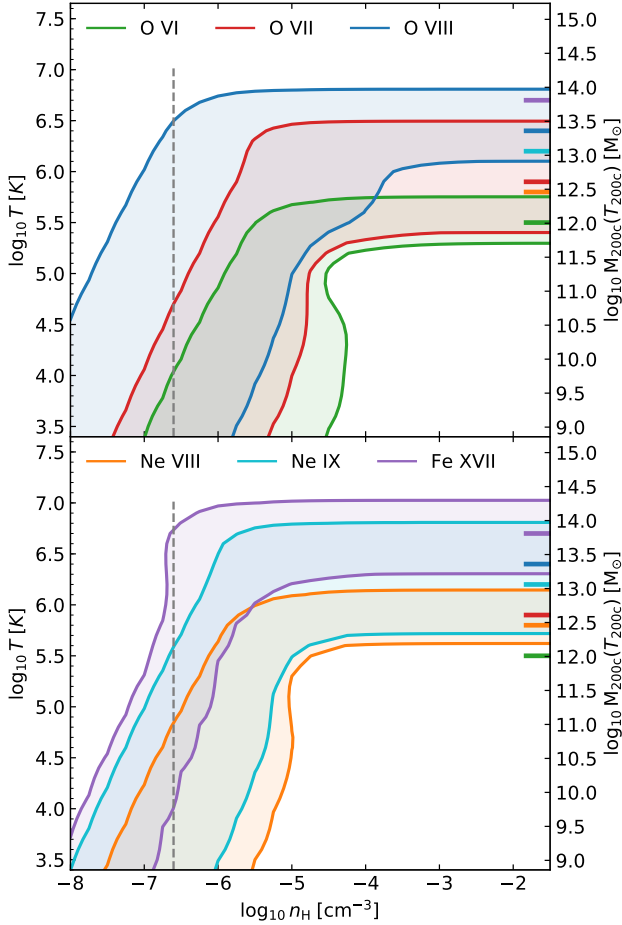


Figure 1. The temperatures and densities where different ions occur at $z = 0.1$, assuming a [Haardt & Madau \(2001\)](#) UV/X-ray background as the only photo-ionizing source. The contours for each of the indicated ions are at 10 per cent of the maximum ion fraction in CIE. The vertical, dashed line indicates the cosmic average baryon density. The right axis indicates the halo masses with virial temperatures (eq. 3) matching the temperatures on the y-axis, and the coloured ticks indicate where each ion’s fraction peaks in CIE.

The O VII and O VIII panels are similar to fig. 5 of [Wijers et al. \(2019\)](#), and we compute the EWs for the other ions in mostly the same way, using `specwiz` (e.g., [Tepper-García et al. 2011](#), §3.1). Briefly, in [Wijers et al. \(2019\)](#) we extracted absorption spectra along 100 cMpc sightlines through the full EAGLE simulation box, then calculated the EW for the whole sightline, and compared that to the total column density calculated in the same code.

In `SPECWIZARD`, sightlines are divided into pixels (1-dimensional), and ion densities, ion-weighted peculiar velocities and ion-weighted temperatures are calculated in those pixels. The spectrum is then calculated by adding up the optical depth contributions from the position-space pixels in each spectral pixel. The optical depth profile used for each position-space pixel is Gaussian, with the centre determined by the pixel position and peculiar velocity, the width by the temperature (thermal line broadening only), and the normalization by the column density. Since, in reality, spectral

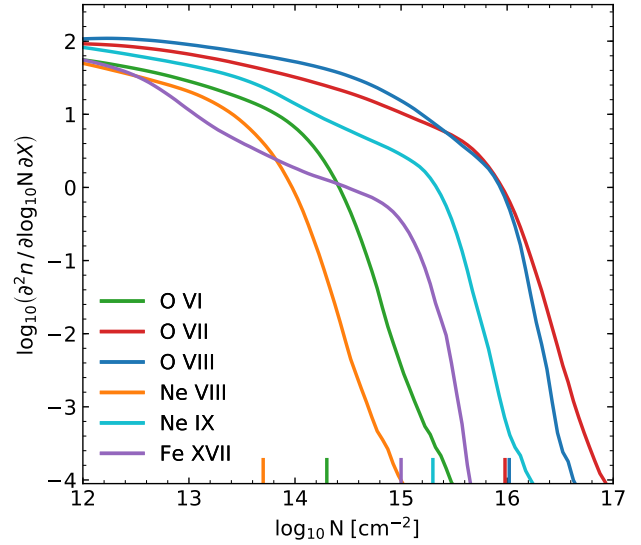


Figure 2. The CDDFs for the ions we consider in this paper. Coloured ticks on the x-axis roughly indicate the positions of breaks in the CDDFs (determined visually), which serve as reference points in further figures. These are at the same position for O VII and O VIII, but the ticks are slightly offset for legibility.

lines are better described as Voigt profiles, a convolution of a Gaussian with a Cauchy-Lorentz profile, we convolve the (Gaussian-line) spectra from `SPECWIZARD` with the appropriate Cauchy-Lorentz profile for each spectral line, using the transition probabilities from Table 2.

Comparing EWs calculated over the full sightlines with and without the additional line broadening (eq. 5), we find that for O VI and Ne VIII, the differences are < 0.01 dex everywhere. For the X-ray ions, the vast majority of sightlines show differences < 0.1 dex, with larger differences occurring in $\lesssim 10$ sightlines at the highest column densities. The differences are largest for Fe XVII.

In Fig. 3, we do not measure column densities and EWs along full 100 cMpc sightlines. Instead, we use velocity windows around the line-of-sight velocity where the optical depth is largest. These velocity windows are indicated in Fig. 3 as the maximum velocity to the maximum optical depth location, which is half the total velocity range considered. We calculate EWs in these velocity ranges by integrating the synthetic spectra over that velocity range. For the column densities in those windows, we use the fact that the total optical depth is proportional to the column density. Therefore, the fraction of the total column density in each velocity window is the same as the fraction of the total integrated optical depth contained within the window.

Note that we do not necessarily use all absorption systems in the sightline. This may bias our results, but so does using full sightline values. Identifying and fitting individual absorbers and absorption systems is beyond the scope of this paper. In appendix A, we show that our results are insensitive to the precise choice of velocity window.

For the UV ions, we mimic velocity windows used to define absorption systems by observers: $\pm 300 \text{ km s}^{-1}$ (rest-frame). This matches how [Burchett et al. \(2019\)](#) defined absorption systems in their CASBaH study of Ne VIII. For

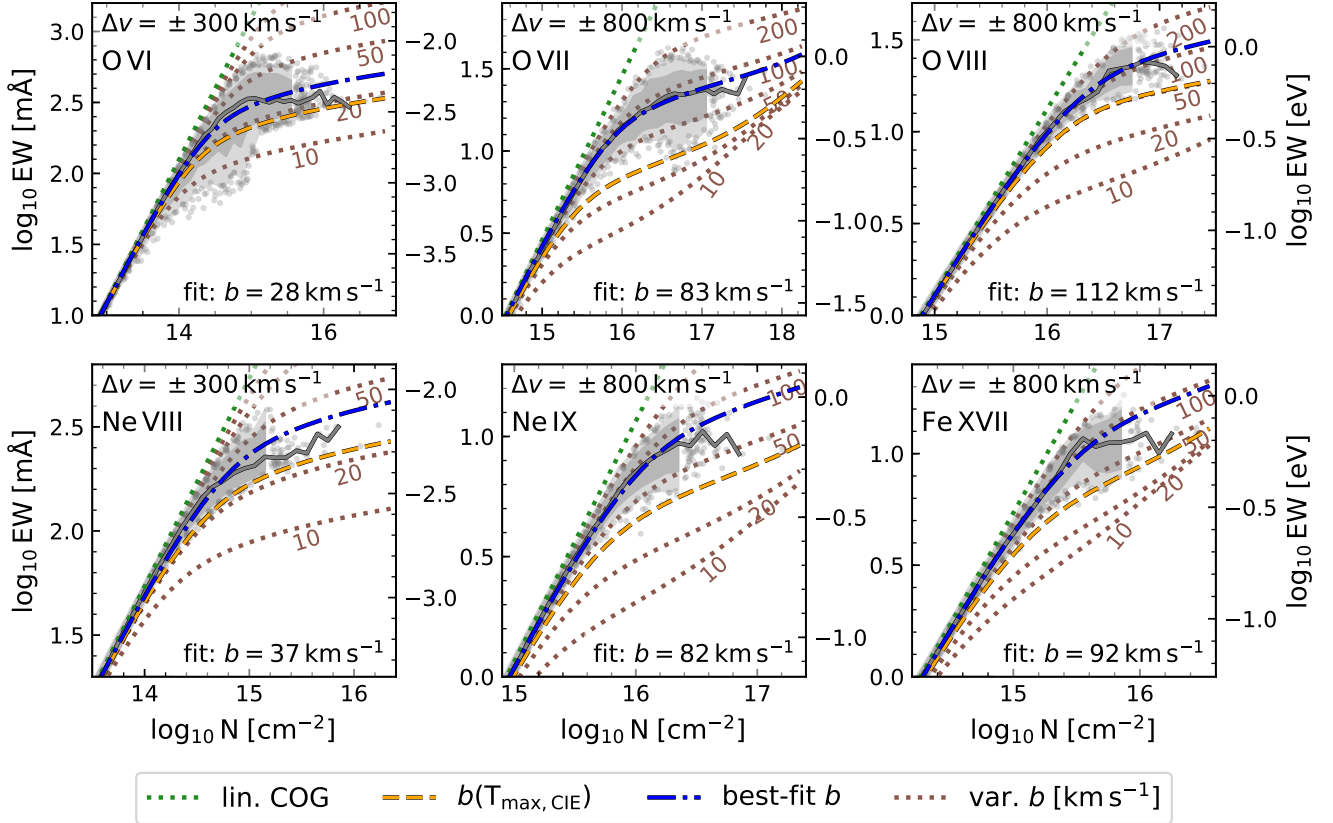


Figure 3. Rest-frame EWs for the ions we investigate as a function of ion column density. The left axes show EWs in \log_{10} mÅ, the right axes show \log_{10} eV. The solid, grey line shows the median EW in bins of 0.1 dex in column density, while the shading shows the central 80 per cent (darker grey) and central 96 per cent (lighter grey) of the EWs in the bins. For EWs outside these ranges, and column density bins with fewer than 50 sightlines, we show each sightline as a single grey point. We also show best-fit values (using eq. 6) for the Gaussian line broadening b (eq. 4) in blue dot-dashed lines. The best-fit values are indicated in the bottom right of each panel. The relation for unsaturated absorption is shown with a dotted green line. The orange, dashed line shows the thermal broadening for ions at the temperature where their ion fraction is at a maximum in CIE (equation 7, Fig. 1). The various dotted brown lines show the column-density-EW relation for Voigt profiles with different Gaussian line broadening values (i.e., b parameters): 10, 20, 50, 100, and 200 km s^{-1} , from bottom to top in the panels. The spectra and column-density-EW relations are for absorption lines at a single rest-frame wavelength, except for O VIII, where we model doublet absorption.

O VI, Johnson et al. (2015) searched $\Delta v = \pm 300 \text{ km s}^{-1}$ regions around galaxy redshifts for the eCGM survey. Tumlinson et al. (2011) searched a larger region of $\Delta v = \pm 600 \text{ km s}^{-1}$ in the COS-Halos survey, but found that the absorbers were strongly clustered within $\Delta v = \pm 200 \text{ km s}^{-1}$. Note that that this does not mean the indicative b -parameters we find here from the curve of growth should be directly compared with observed values: in UV observations, line widths are often measured by fitting Voigt profiles to individual absorption components, instead of inferred from theoretically known column densities and EWs of whole absorption systems as we do here.

For the X-ray lines, we want to use velocity windows resolvable by the Athena X-IFU: the FWHM resolution should be 2.5 eV (Barret et al. 2018). This corresponds to different velocity windows for the different lines (at different energies) we consider: $\approx 1200 \text{ km s}^{-1}$ for O VII, 1000 km s^{-1} for O VIII, 800 km s^{-1} for Fe XVII, and 700 km s^{-1} for Ne IX

at $z = 0.1$. Based on the dependence of the best-fit b -parameters on the velocity ranges, we choose to use a half-width $\Delta v = \pm 800 \text{ km s}^{-1}$ for the X-ray ions. We discuss this choice in appendix A.

We started with the sample of spectra for the sightlines used in Wijers et al. (2019) for $z = 0.1$. This sample was a combination of three subsamples, selected to have high column density in O VI, O VII, or O VIII. Subsamples were selected uniformly in log column density for $N \geq 10^{13} \text{ cm}^{-2}$ in each ion, iterating the selection until the desired total sample size of 16384 sightlines was reached. For this work, we added a sample of the same size, but with subsamples selected by Ne VIII, Ne IX, and Fe XVII column density. Some sightlines in the two samples overlapped, giving us a total sample of 31706 sightlines. In Fig. 3, we show the column densities and equivalent widths for each ion using that ion's subsample. The subsamples contain ≈ 5600 sightlines each.

Table 2 lists the wavelengths, oscillator strengths, and

Table 3. Best-fit b parameters to the column-density-EW relation for the different ions. Rest-frame EWs are calculated for each ion (first column) using the absorption lines in Table 2. The second column indicates the half width of the velocity windows used to calculate the EWs. Column 3 shows the best-fit b parameters, using the velocity windows in column 2. The fits are to log EWs.

ion	$\Delta\nu$ km s ⁻¹	$b(\Delta\nu)$ km s ⁻¹
O VI	300	28
Ne VIII	300	37
O VII	800	83
Ne IX	800	82
O VIII	800	112
Fe XVII	800	92

transition probabilities we use for the ions. If an ion absorption line is actually a close doublet (expected to be unresolved), we calculate the equivalent widths from the total spectrum of the doublet lines. This is only the case for O VIII (e.g. fig. 4 of [Wijers et al. 2019](#)). For Fe XVII, the 15.26, 15.02 Å doublet has a rest-frame velocity difference of 4.75×10^3 km s⁻¹. This is well above the line widths we find, so the lines will not generally be intrinsically blended, and should be resolvable by the Chandra LETG¹ and the XMM-Newton RGS ([den Herder et al. 2001](#), fig. 11). The Athena X-IFU will have a higher resolution ([Barret et al. 2018](#)). We only use the stronger component for the O VI 1031.9, 1037.6 Å and Ne VIII 770.4, 780.3 Å doublets, which are easily resolved with current FUV spectrographs.

We note that for Fe XVII, the atomic data for the line are under debate, with theoretical calculations and experiments finding different values (e.g., [Gu et al. 2007](#); [de Plaa et al. 2012](#); [Bernitt et al. 2012](#); [Wu & Gao 2019](#); [Gu et al. 2019](#)). Indeed the [Kaastra \(2018\)](#) wavelength and oscillator strength that we use for this ion do not agree with the [Verner et al. \(1996\)](#) values. The wavelengths only differ by 0.001 Å (a relative difference of 0.007 per cent), but the oscillator strengths and transition probabilities differ by 8 per cent.

In Fig. 3, we also show indicative relations between the column density and EW (so-called ‘curves of growth’), parametrized by line widths b . These relations are for a single Voigt profile (or doublet of Voigt profiles). They consist of a Gaussian absorption line convolved with a Cauchy-Lorentz profile. The line is described by a continuum-normalized spectrum $\exp(-\tau(\Delta\nu))$, where $\Delta\nu$ is the velocity offset from the line centre and τ is the optical depth. The Gaussian part of the optical depth profiles is described by

$$\tau(\Delta\nu) \propto N b^{-1} \exp\left(-(\Delta\nu b^{-1})^2\right), \quad (4)$$

where N is the column density of the ion. The constant of proportionality is governed by the atomic physics of the transition in question. For such a line, FWHM = $1.67b$. However, the line is additionally broadened by the Cauchy-Lorentz component

$$f(\nu) = \frac{1}{4\pi^2} \frac{A}{(\Delta\nu)^2 + (A/4\pi)^2}, \quad (5)$$

where $\Delta\nu$ is the frequency offset and A is the transition probability. When we fit b parameters, we model the Voigt profile of the lines (convolution of eqs. 4 and 5), and b refers to the width of the Gaussian component (eq. 4) alone.

In Table 3, we show these b parameters fit to the column densities and EWs measured along the different sightlines for the different ions. Column 3 shows fits to the column densities and EWs calculated over the velocity windows in column 2. The fits in columns 3 are obtained by minimizing

$$\sum_i (\log_{10} \text{EW}_i - \log_{10} \text{EW}(N_i, b))^2, \quad (6)$$

where the sum is over the sightlines, N is the column density, and $\text{EW}(N, b)$ is obtained by integrating the spectrum produced by the Voigt profile in eqs. 4 and 5. The values from column 3 are used in Fig. 3. Fitting the EWs themselves instead of the log EWs makes little difference: only a few km s⁻¹. Using the velocity windows instead of the full sightlines only makes a substantial difference for O VIII. We discuss the dependence of the best-fit b values on the velocity range used in appendix A.

The shadings in Fig. 3 gives an indication of how broad the b -parameter distribution is (10th and 90th, 2nd and 98th percentiles). Generally, the thermal line broadening expected at the temperature where the ion fraction peaks in CIE,

$$b(T_{\text{max,CIE}}) = \sqrt{2kT_{\text{max,CIE}} m_{\text{ion}}^{-1}}, \quad (7)$$

gives a good lower limit to the EWs (dashed orange lines). Here, m_{ion} is the ion mass. For O VII, Ne IX, Fe XVII, and particularly O VI, lower values do occur. For O VII, Ne IX, and Fe XVII, this is still consistent with the lower end of the CIE temperature range in Table 1: $b = 16, 20$, and 24 km s⁻¹, respectively. For O VII, this was previously described by [Wijers et al. \(2019\)](#). For O VI, the lower CIE end gives $b = 14$ km s⁻¹, which does not cover this range. Such low b values are rare for this ion, but their occurrence suggests at least some high-column-density O VI is photo-ionised.

3.2 Haloes and the column density distribution

Next, we look into how the ions relate to haloes. Fig. 4 shows the contributions of haloes of different masses to the total mass and ion budget in the simulated 100^3 cMpc³. An SPH particle is considered part of a halo if it is within the halo’s FoF group or R_{200c} region. We include the 14.5–15 bin for consistent spacing, but this bin contains only a single halo with $M_{200c} = 10^{14.53} M_{\odot}$, so in rest of the paper, we will group all nine haloes with masses $M_{200c} \geq 10^{14} M_{\odot}$ into one halo mass bin.

For the metal ions, as we will see later in Fig. 13, the temperatures and densities of gas contributing to the ion budget do not differ very much between haloes of different masses, as the densities follow profiles that are similar between different haloes, and the ions mostly trace whatever gas is near their CIE temperatures. The virial temperatures of the haloes determine how much of the halo gas is at those temperatures. This results in ion budgets that are dominated by halo masses where $T_{200c} \sim T_{\text{CIE}}$.

¹ http://cxc.harvard.edu/cdo/about_chandra/

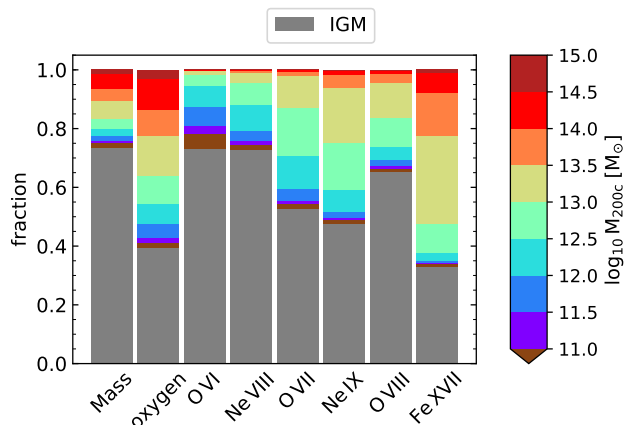


Figure 4. The fraction of total gas mass and the (gas-phase) elements and ions we investigate contributed by haloes of different masses. Colours indicate halo masses according to the colour bar, with grey indicating gas that does not belong to any halo. Neon and iron (not shown) are distributed similarly to oxygen.

We now move from the ion distribution to the absorber distribution. Fig. 5 shows the contributions of different halo masses to the CDDFs of our six ions. The CDDFs for each halo mass bin are generated from the simulations in the same way as the total CDDFs, but using only SPH particles belonging to a halo of that mass. An SPH particle belongs to a halo if it is in the halo’s FoF group, or within R_{200c} of the halo centre.

From Fig. 5, we see that for the X-ray ions, most absorption at column densities higher than the knee of the CDDF is due to haloes. This confirms the suspicion of Wijers et al. (2019) that this was the case for O VII and O VIII, based on the typical gas overdensity of absorption systems at these column densities. However, for the FUV/EUV ions O VI and Ne VIII, there is a substantial contribution from gas outside haloes at these relatively high column densities.

For all these ions, we also note the following trend. The absorption at higher column densities tends to be dominated by more massive haloes until a turn-around is reached. These turn-around masses are consistent with the temperatures preferred by the ions, suggesting they are being driven by the increase in virial temperature with halo mass (compare to Fig. 1). We have verified that trends with halo mass are not driven simply by the covering fraction of haloes of different masses.

Based on the CDDFs for gas coming from haloes of different masses, we can estimate how many haloes of different masses should be detectable with the Athena X-IFU over a given total redshift path dz . Here, it does matter if we use the CDDFs based on FoF-gas-only column density maps (such as in Fig. 5), or maps including all gas, but only counting pixels with impact parameter $r_{\perp} \leq R_{200c}$, and that are not closer to another halo in r_{\perp}/R_{200c} units (see Appendix B).

Using estimated minimum column densities of $10^{15.4} \text{ cm}^{-2}$ for O VII and $10^{15.6} \text{ cm}^{-2}$ for O VIII (based on a minimum observed EW of 0.18 eV, Lumb et al. 2017), we expect to find, in total, 2.3 O VII absorbers and 1.0 O VIII absorbers per unit redshift. Of those, 46 and 63 per cent are

within R_{200c} of a central galaxy with $M_{200c} > 10^{11} M_{\odot}$, respectively. For O VII, 41 per cent of all the absorbers is attributed to haloes with $M_{200c} = 10^{12}-10^{13.5} M_{\odot}$, and for O VIII, 53 per cent comes from $M_{200c} = 10^{12.5}-10^{13.5} M_{\odot}$ haloes. (Since the FoF-only CDDFs do not add up to the all-gas CDDF, we do not attempt to derive such fractions from the FoF-only CDDFs.)

We also estimate the total density along lines of sight of observable absorbers coming from haloes of different masses. Here, both the FoF-mass-only CDDFs and the all-gas, $r_{\perp} \leq R_{200c}$ CDDFs are reasonable starting points. Based on these two kinds of CDDFs, we expect to find 0.30 (0.34), 0.39 (0.61), and 0.26 (0.42) O VII absorbers per unit redshift with the Athena X-IFU blind survey based on the all-gas, $r_{\perp} \leq R_{200c}$ CDDFs (based on the FoF-only CDDFs), in haloes of $M_{200c} = 10^{12}-10^{12.5}$, $10^{12.5}-10^{13}$, and $10^{13}-10^{13.5} M_{\odot}$, respectively. For O VIII, we similarly expect 0.21 (0.20) and 0.31 (0.37) absorbers per unit redshift in M_{200c} bins of $10^{12.5}-10^{13}$ and $10^{13}-10^{13.5} M_{\odot}$, respectively. This is assuming most of the redshift path searched is close to $z = 0.1$, which is the redshift of the EAGLE snapshot we extracted the CDDFs from. We compare the the absorption to $z = 0.5$ in Appendix C.

Therefore, halo absorbers seem to be somewhat rare, but in a search for O VII and O VIII absorbers against 100 BLLacs and 100 gamma ray bursts, we can reasonably expect to find quite a few of these absorbers. There are differences between the different determinations of halo absorption, but they are mostly not too severe. We have also assumed that a single limiting column density is a good estimate for detectability of these absorbers. We can see from Fig. 3, and fig. B1 of Wijers et al. (2019), that this should be a reasonable approximation for the limiting-case absorption lines.

3.3 Column density profiles for different halo masses

We now switch perspectives, and consider what we might find if we looked for absorption around haloes of different masses. For this, we use the radial profiles computed as described in §2.3. Table 4 shows the sample size we use for different halo masses. The column density radial profiles are shown in Fig. 6. The solid lines show absorption by all gas in the same 6.25 cMpc slice as the halo centres, while the dashed lines show absorption only by gas in a halo (FoF group or otherwise inside R_{200c}) with M_{200c} in the matched halo mass range. In principle, this means that single-halo profiles might include absorption by gas in different haloes of similar mass, but the fact that the dashed lines for all ions drop off sharply at the same $r_{\perp} \approx 1.5 R_{200c}$ indicates that this effect is negligible, at least for the median profiles.

We see a clear pattern: the median column density increases with halo mass until it reaches a peak, which corresponds to the halo mass where the relative contribution to the CDDF (at higher column densities) peaks in Fig. 5. This again supports the idea that the column densities of these haloes are largely driven by the halo virial temperature.

We also note more qualitative trends. Column densities at large distances ($\gtrsim 2 R_{200c}$) increase considerably less with halo mass than central column densities do. At halo masses beyond the peak, the median column density declines and

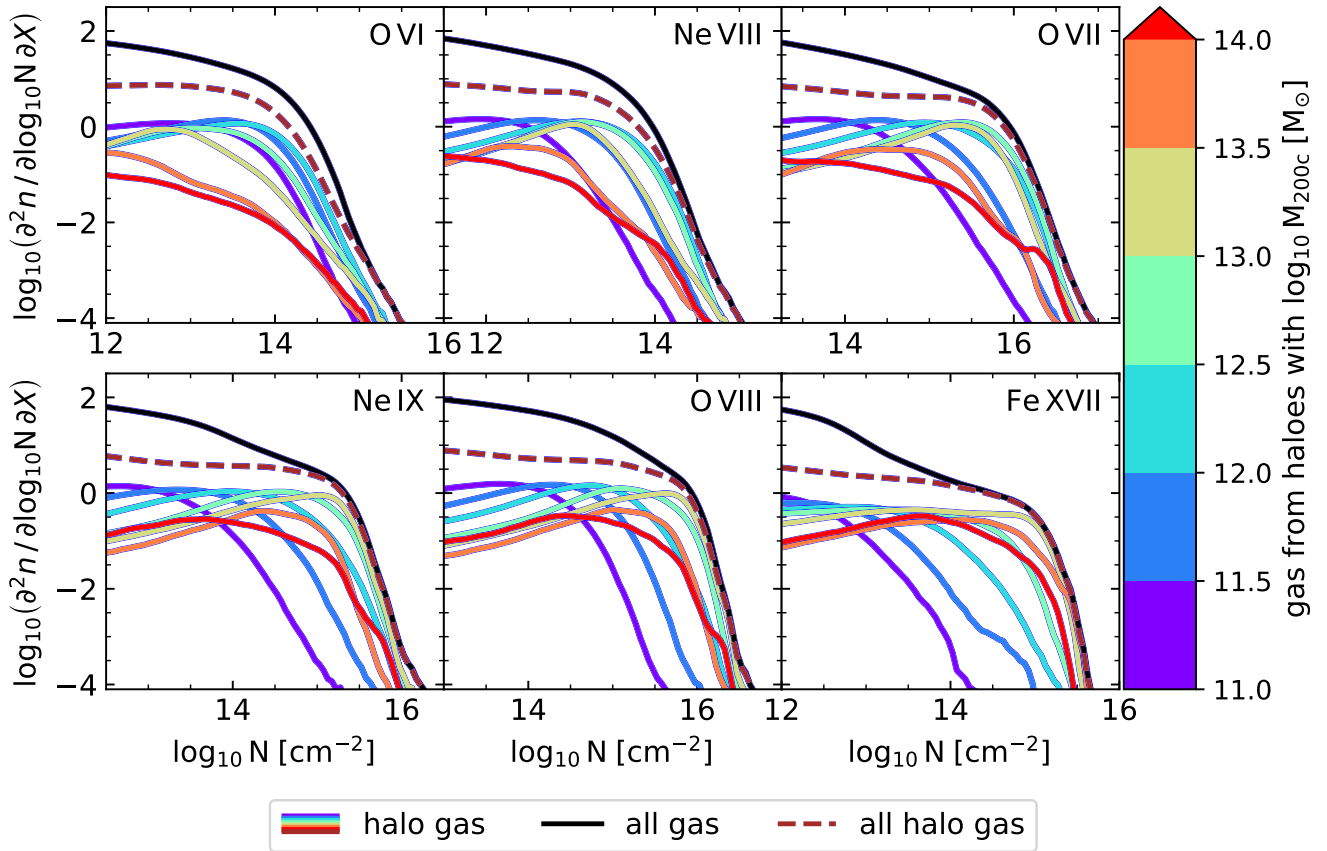


Figure 5. The contribution of absorption by haloes of different masses to the column density distributions of the ions indicated in the panels. The black line indicates the distribution of all absorption systems, while the brown, dashed line indicates the contribution of all haloes (including those with $M_{200c} < 10^{11} M_{\odot}$). The colour bar indicates the mass range for which each solid, coloured line represents the contribution to the CDDF. Contributions are determined by computing CDDFs from column density maps made with only gas in each halo mass range.

Table 4. The halo sample size from L0100N1504 at $z = 0.1$, with the total number of haloes (equal to the number used for the 2D radial profiles), the number outside R_{200c} of any 6.25 cMpc slice edge, and the number used for 3D radial profiles.

M_{200c} $\log_{10} M_{\odot}$	total	off edges	3D profiles
11.0–11.5	6295	6044	1000
11.5–12.0	2287	2159	1000
12.0–12.5	870	792	870
12.5–13.0	323	288	323
13.0–13.5	119	103	119
13.5–14.0	26	20	26
≥ 14.0	9	8	9

the profile flattens within R_{200c} , even having a deficit of absorption somewhere in the range ~ 0.1 – $1 R_{200c}$ compared to $\sim R_{200c}$ for the lower-energy ions in the largest halo mass bins. We will examine the causes of these trends in §3.5, using (3D) radial profiles of the halo gas properties.

The fraction of absorption caused by gas in the haloes

(dashed curves) also shows a clear trend: the halo contributions are largest in halo centres, and for haloes at the mass where the median column density peaks. Halo contributions drop as typical column densities decrease, towards both higher and lower halo masses.

Comparing to the column densities where breaks in the CDDFs occur (long horizontal grey ticks on the left), we see the absorption in the high column density tails of the overall distribution, at column densities above those indicated, comes from absorbers that are stronger than typical for haloes of any mass. Therefore, the low occurrence of stronger absorbers does not simply reflect the low volume density of haloes in the ion’s preferred mass range, it is also due to the fact that they are relatively high column density absorbers for such haloes. Note that the scatter here includes both inter-halo and intra-halo scatter, so it is possible that such absorbers are more common in a subset of haloes at some halo mass.

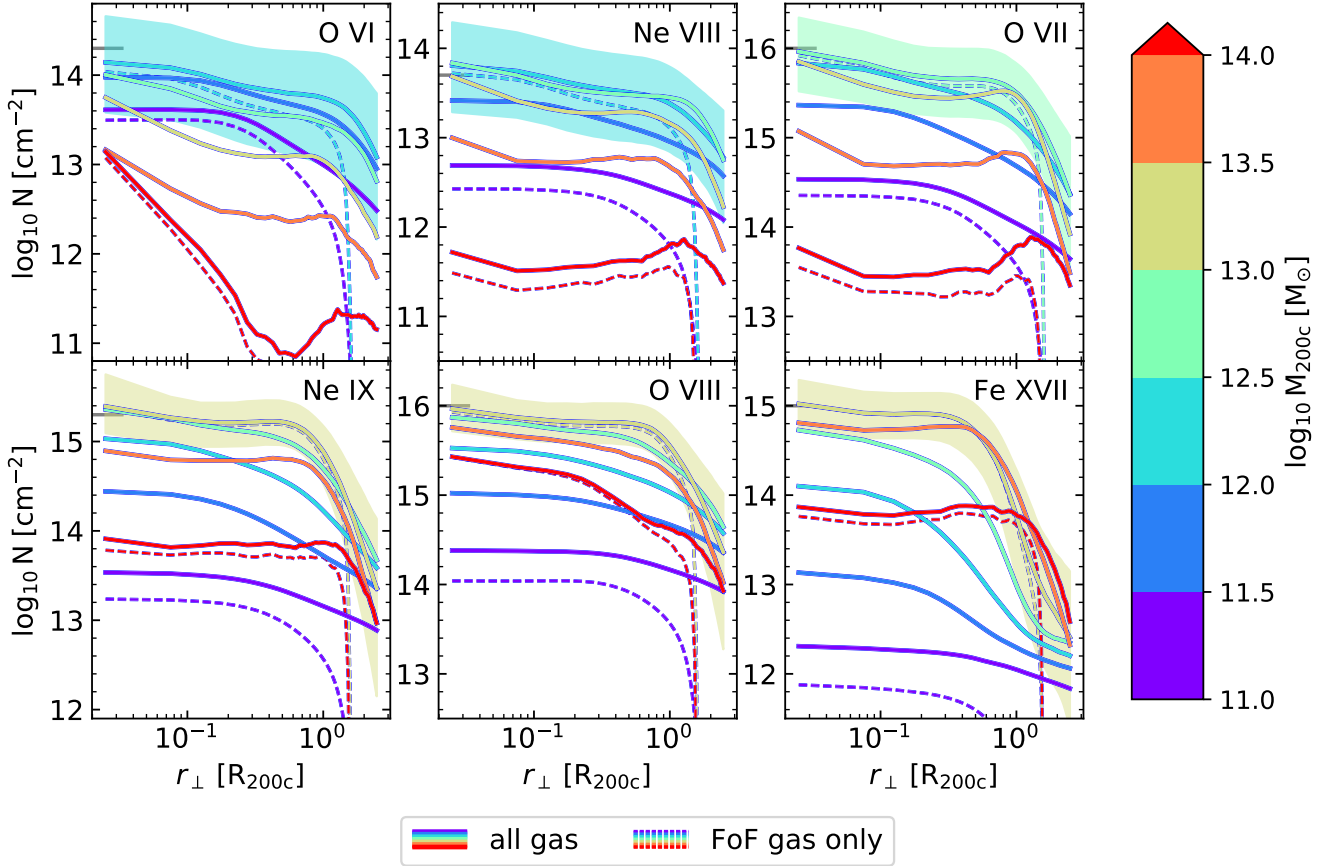


Figure 6. Radial column density profiles for the different ions around central galaxies in haloes of different masses. The median column density at different impact parameters is shown, with shaded regions showing the 10th–90th percentile range for a halo mass bin with a high central peak column density. Column densities are measured in the single 6.25 cMpc slice of the box that contains each central galaxy’s centre of mass. The grey ticks indicate roughly where breaks in the CDDFs for the different ions occur (see Fig. 2). Solid lines include all gas from a given slice, while dashed lines show absorption around haloes in each slice coming only from gas within haloes (FoF group or within R_{200c}) in the same M_{200c} range. For legibility, we only show the halo contributions for three halo mass bins: the mass yielding the maximum median column density for each ion, and the highest and lowest masses.

3.4 The baryon content of halos

To help explain the column density profiles we found, we look into the intrinsic physical properties of haloes of different masses. We consider halo averages in this section, and well as properties as a function of (3D) distance to the halo centre in §3.5. For both averages and 3D radial profiles for $M_{\odot} < 10^{12} M_{\odot}$ haloes, we use a subsample of 1000 randomly selected haloes in each 0.5 dex mass bin, in order to reduce the computational cost of the calculations while maintaining a large sample size.

We start by looking into the baryon and metal content in haloes of different masses. Fig. 7 shows the mass fraction in different baryonic components as a function of halo mass. The black hole contribution is too small to appear on the plot. The total baryon fraction increases with halo mass, and is substantially smaller than the cosmic fraction for $M_{200c} < 10^{13} M_{\odot}$. The trend at lower halo masses ($M_{500c} < 10^{13} M_{\odot}$) is not currently constrained by observations. The EAGLE baryons fractions are somewhat too high

for $M_{200c} > 10^{14} M_{\odot}$ (Barnes et al. 2017). The observations do support the trend of rising baryon fractions with halo mass at high masses.

The CGM mass fraction increases with halo mass, while the stellar and ISM fractions peak at $M_{200c} \sim 10^{12} M_{\odot}$, with the ISM fraction declining particularly steeply towards higher masses. This is likely a result of star formation quenching starting in $\sim L_*$ galaxies. The ‘missing baryons’ CGM at $10^{5.5}$ – 10^7 K dominates for halo masses $M_{200c} \sim 10^{12}$ – $10^{13.5} M_{\odot}$, which is what we would expect according to T_{200c} . The $M_{200c} \sim 10^{12}$ – $10^{13.5} M_{\odot}$ haloes where this gas dominates are indeed the ones that dominate the ion budgets in Fig. 4, except for O VI, which probes cooler gas, and Fe XVII, which probes gas in this temperature range, but where the dominant haloes include some higher-mass ones, in agreement with T_{200c} (Fig. 1).

Fig. 8 similarly shows the fraction of oxygen in different baryon components for haloes of different masses. Oxygen produced in stars, but never ejected is not counted. A smaller

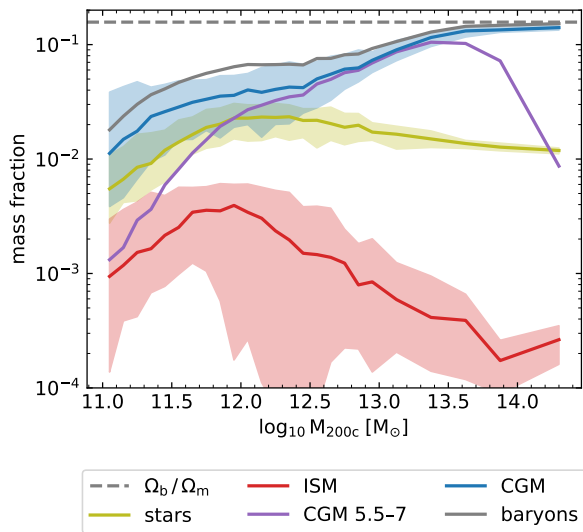


Figure 7. The fraction of halo mass (i.e., $< R_{200c}$) in stars, ISM, and CGM as a function of halo mass. Here, ISM is defined as all star-forming gas and CGM as the other gas. The gray line shows the total baryon mass fraction, and the purple line shows CGM gas with temperatures in the $10^{5.5}-10^7$ K range. The solid lines show medians and shaded regions show the 80 per cent halo-to-halo scatter in each halo mass bin; the shading is omitted for legibility for the total baryons and $10^{5.5}-10^7$ K CGM. The dashed line indicates the cosmic baryon fraction. We use 0.1 dex halo mass bins for $M_{200c} < 10^{13} M_{\odot}$ haloes, then 0.25 dex bins, and one bin for the haloes above $10^{14} M_{\odot}$.

fraction of the oxygen that was swallowed by black holes is not tracked in EAGLE. The fraction in stars therefore reflects the metallicity of the gas the stars were born with. The fractions for neon are nearly identical to those for oxygen, while the curves for iron have the same shape, but with a somewhat smaller mass fraction in stars and more in CGM and ISM.

We see that at lower halo masses, most of the metals in haloes reside in stars, while for $M_{200c} \gtrsim 10^{13} M_{\odot}$, more metals are found in the CGM. The changes with halo mass seem to be in line with the overall mass changes in ISM and CGM as halo mass increases (Fig. 7), though the stars and ISM contain higher metal fractions than mass fractions, reflecting their higher metallicities. Interestingly, there are more metals in the CGM than in the ISM for all halo masses, though the difference is small for $M_{200c} < 10^{12} M_{\odot}$. This is similar to what [Oppenheimer et al. \(2016\)](#) found for a smaller set of haloes with EAGLE-based halo zoom simulations. They considered all the oxygen produced in galaxies within R_{200c} , in 20 zoom simulations of $M_{200c} = 10^{11}-10^{13} M_{\odot}$ haloes, and found that a substantial fraction of that oxygen ($\sim 30-70$ per cent) is outside R_{200c} at $z = 0.2$. That oxygen is not included in the census in Fig. 8.

The mass and oxygen fractions in the CGM and ISM do depend somewhat on the definition of the ISM. In Figs. 7 and 8, we define the ISM as all gas with a non-zero star formation rate. Since the minimum density for star formation in EAGLE is lower for higher metallicity, higher-metallicity gas is more likely to be counted as part of the ISM. If we define

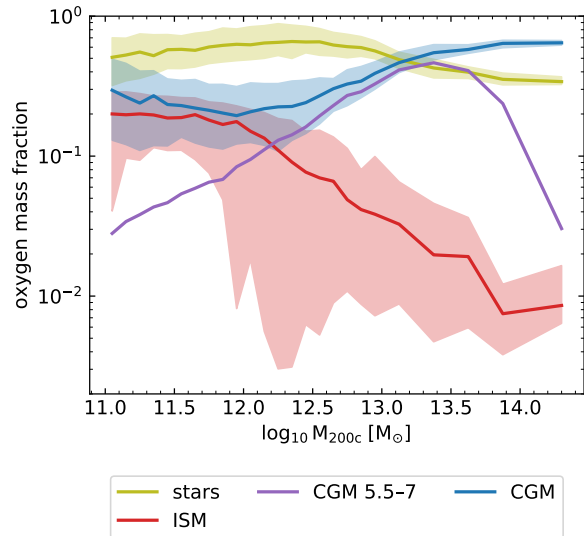


Figure 8. The median fraction of halo oxygen mass (oxygen ejected by stars, currently within R_{200c}) in stars, ISM, and CGM in haloes of different masses. Here, ISM is defined as all star-forming gas and CGM as the other gas. The purple line shows CGM gas with temperatures in the $10^{5.5}-10^7$ K range. The shaded regions show the 80 per cent halo-to-halo scatter in each halo mass bin; the shading is omitted for legibility for the $10^{5.5}-10^7$ K CGM. The halo oxygen budget (total and in stars) does not include metals produced in stars that have never been ejected, or any oxygen captured by black holes.

the ISM as gas with $n_H > 10^{-1} \text{ cm}^{-3}$ instead, the mass fractions change. Per halo, the ISM mass changes by a median of $\sim -30-50$ per cent for $M_{200c} \lesssim 10^{12} M_{\odot}$, ≈ 0 per cent at $\sim 10^{13} M_{\odot}$, and up to $+30$ per cent at higher masses. The central 80 per cent range is large, including differences comparable to the total ISM mass using the star-formation definition in both directions. The scatter in differences is largest at low masses. The median trend with halo mass makes sense given the higher central metallicities (meaning lower minimum n_H for star formation) we find in lower-mass haloes (Fig. 12). If we count gas that is star-forming or meets the n_H threshold as ISM, the ISM mass can only increase relative to the star-forming definition. Median differences are $\lesssim 3$ per cent at $M_{200c} \lesssim 10^{12} M_{\odot}$, but increase to $\approx 30-60$ per cent at $M_{200c} \gtrsim 10^{13} M_{\odot}$. Since the CGM contains more mass overall, differences in the CGM mass using the two alternative ISM definitions are typically $\lesssim 11$ per cent (central 80 per cent of differences).

The ISM definitions also affect how oxygen is split between the ISM and CGM. Using the $n_H > 10^{-1} \text{ cm}^{-3}$ definition results in lower ISM oxygen fractions, with median per-halo differences $\approx -20-55$ per cent, and a central 80 per cent range of differences mostly between ≈ -10 and -90 per cent. CGM fractions are consistently higher, with median per-halo differences of up to ≈ 40 per cent at $M_{200c} < 10^{12.5} M_{\odot}$, decreasing to close to zero between $M_{200c} = 10^{12}$ and $10^{13} M_{\odot}$. Using the combination ISM definition ($n_H > 10^{-1} \text{ cm}^{-3}$ or star-forming) does not change the oxygen masses by much, since dense, but non-star-forming

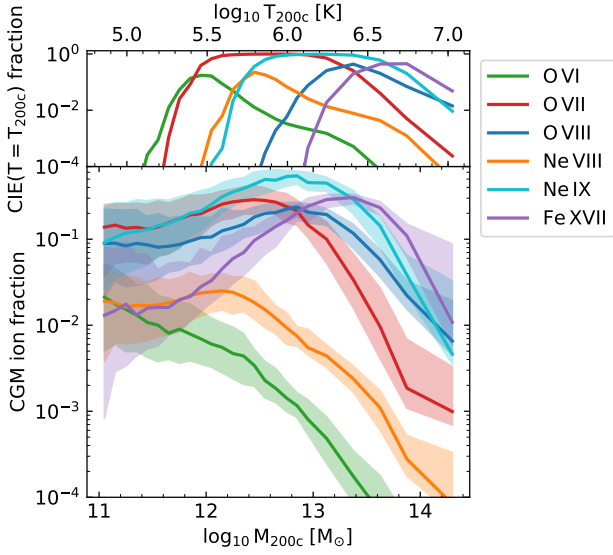


Figure 9. Total fraction of each element in the ionization states we focus on in this work, in the CGM ($0.1\text{--}1 R_{200c}$; lower panel). The solid lines show median ion fractions in different mass bins, while the shaded regions in the same colour show the scatter (percentiles 10–90). The top panel shows the CIE ion fractions as a function of temperature, assuming the temperatures match T_{200c} for the different halo masses. The virial temperature and CIE ionization curves predict the qualitative trends of ionization fraction as a function of halo mass, but strongly underestimate the ion fractions in low-mass haloes.

gas has a low metallicity. The central 80 per cent of per halo differences is < 1 per cent at all M_{200c} .

Next, we look into the ionization state of haloes of different mass.² The bottom panel of Fig. 9 shows the fraction of ions in the CGM (in the $0.1\text{--}1 R_{200c}$ range) as a function of halo mass, and compares it to the CIE ion fraction at the halo virial temperatures in the top panel. Including the gas within $0.1 R_{200c}$ has a negligible effect, since there is very little gas there (Fig. 11). Including gas out to $2 R_{200c}$ does make a difference. If that gas is included, these ion fractions rise, especially at the low- and high-mass ends, and the peaks of the ionization curves shift to slightly higher masses. The larger overall ion fractions are likely due to the increased

² Here, for the oxygen species, we use a slightly different set of ionization tables from the rest of the paper. That is because the main set of tables we use does not include all the ionization states of oxygen, and we want to examine the overall partition of oxygen ion fractions in haloes. This second set of tables was made under the same assumptions as our main set: the uniform but time-dependent UV/X-ray background (Haardt & Madau 2001) used for the EAGLE cooling tables, assuming optically thin gas in ionization equilibrium. However, they were generated using a newer CLOUDY version: 13 (Ferland et al. 2013). We checked by comparing the tables and a smaller EAGLE simulation that the differences between these tables are small for O VI–VIII. In a part of a smaller EAGLE volume, and in the column density regimes of interest, the O VI column densities differed by $\lesssim 0.1$ dex. The O VII and O VIII column densities differed even less. The tables differ most clearly in the photo-ionized regime, where the column densities are small.

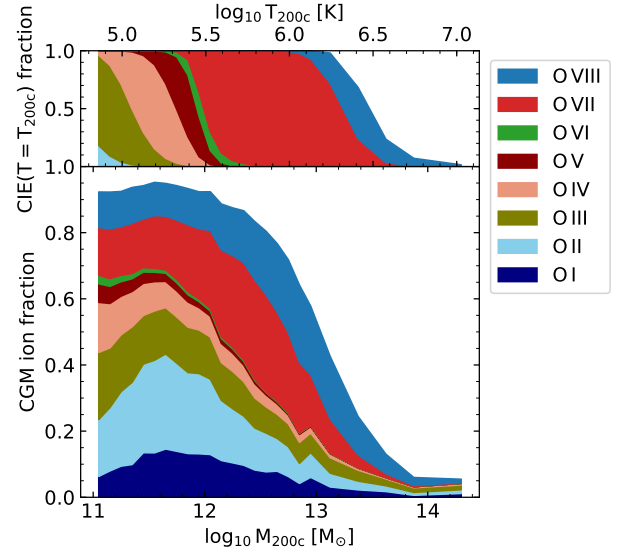


Figure 10. Average fraction of oxygen in the indicated ionization states in the CGM ($0.1\text{--}1 R_{200c}$). In the bottom panel, ions O I–VIII are shown bottom to top in order. In the top panel, we show the CIE ion fractions at the corresponding halo virial temperatures (eq. 3).

amount of gas photo-ionized to the higher states we examine here at larger distances. The slight shifts are likely due to the lower gas temperatures in the same haloes at larger distances (Fig. 12).

Comparing to the CIE ionization curves, we confirm that the CIE ionization peak and halo virial temperatures are good predictors of the qualitative trends of halo ion content as a function of halo mass, but the CIE($T = T_{200c}$) curves strongly underestimate the ion fractions at low mass, where photo-ionization dominates.

The CIE curves peak at slightly larger halo masses than EAGLE haloes show, because the temperature inside R_{200c} is typically higher than T_{200c} . We will show this using the mass- and volume-weighted temperature profiles in Fig. 12.

For O VI, we do not find a peak at all in the halo mass range we examine. This is due to photo-ionization becoming important at and below the halo masses where CIE would produce an O VI peak, in the same regime where other halo ion fractions flatten out.

In Fig. 10, we show what fraction of oxygen in the CGM ($0.1\text{--}1 R_{200c}$) is in the different ionization states (bottom panel). We show the average halo ion fraction in each bin. The top panel shows the CIE ion fractions at the virial temperature. Note that the ionization table we use does not include the effects of self-shielding (or local radiation sources), so the lowest ionization state could be underestimated.

Here, whether or not we include gas at radii $< 0.1 R_{200c}$ has more of an effect: including this gas increases the O I and O II content by large amounts; the fraction of the total increases by $\approx 0.2\text{--}0.4$ for $M_{200c} \sim 10^{11}\text{--}10^{12} M_{\odot}$, with the effect decreasing toward higher halo masses. The difference will be due to the fact that the central galaxy contains plenty of cold gas, but very little of the more highly ionized species. (Wijers et al. (2019) verified that the O VII and

O VIII CDDFs are negligibly impacted by whether or not star-forming gas is accounted for.) Including gas at larger radii (out to $2R_{200c}$) increases the fraction of oxygen in the O VI–VIII states, at the cost of gas in lower states, but also at the cost of O IX at $M_{200c} \gtrsim 10^{12} M_{\odot}$.

As we saw in Fig. 9, the CIE curve for a single temperature predicts much more extreme ion fractions than we see in the Eagle haloes. In particular, Fig 10 shows that lower-mass haloes contain many high ions, and that the lowest ionization states peak at much higher masses than CIE($T = T_{200c}$) predicts, suggesting the presence of significant amounts of gas with $T \ll T_{200c}$.

On the other hand, the higher high-ion fractions than suggested by the CIE curves indicate the presence of $T \gg T_{200c}$ gas in sub- L_* haloes. This is likely a result of gas heating by stellar (and at higher masses, AGN) feedback. Temperature distributions indicate this is not only a result of the direct heating of particles due to feedback in EAGLE, but that sub- L_* haloes have smooth mass- and volume-weighted temperature distributions that can extend to $\sim 10^6$ K or somewhat higher at $\sim R_{200c}$.

3.5 Halo gas as a function of radius

Having examined the overall content of the haloes we investigate, we move on to radial trends. In Fig. 11, we show various cumulative 3-D profiles for each halo. These profiles come from stacking individual haloes’ radial mass distributions, after normalizing those distributions to the amount within R_{200c} . This means that the combined profiles reflect typical (ion) mass distributions, without weighting by halo mass, baryon fraction, or halo ionization state.

Most of the ions in these haloes lie in the outer CGM ($r \gtrsim 0.3R_{200c}$). This explains the relatively flat absorption profiles out to $\sim R_{200c}$ in Fig. 6. The S-shaped cumulative profiles at large halo masses explain the second peaks around R_{200c} in the radial profiles of some of the high-mass haloes: most of the lower-energy ions, like O VI, in these haloes lie in a shell at large radii, which leads to a peak in the 2D-projected column densities. The enclosed ion fractions generally fall between the enclosed mass and volume fractions. Exceptions are lower ions in the inner CGM of high-mass haloes. Also, Fe XVII is more centrally concentrated than the other ions and gas overall, as Fig. 6 also showed. We will discuss this in more detail later. The high spike in O VI mass at large radii in low-mass haloes is not present in a small, random sample of individual halo O VI profiles, and is therefore not a typical feature for this halo mass.

In Fig. 12, we show example mass- and volume-weighted median temperature and density profiles. For the temperature profiles, the dotted lines show the simplest prediction: T_{200c} , as calculated from eq. 3. The colours match the median halo mass in each bin. The profiles show a general rising trend with halo mass, with temperatures at R_{200c} matching T_{200c} reasonably, and following the T_{200c} trend. However, the temperature clearly decreases with radius in most cases. The exceptions are the inner parts of the profiles for low-mass haloes, for which the volume-weighted median temperatures can be much higher than the mass-weighted ones. The haloes are in fact multiphase, with cool gas at $\sim 10^4$ K, some gas at $\sim 10^5$ K, and the hotter volume-filling phase. Sharp transitions in the median profiles occur when the median

switches from one phase to another. The multiphase nature is particularly prominent at low mass ($M_{200c} \ll 10^{13} M_{\odot}$).

The gas density also decreases with radius. It is generally higher in higher-mass haloes around R_{200c} , but at larger radii it also drops much faster than in lower-mass systems. Volume-weighted densities can be considerably lower than mass-weighted densities, reflecting the multi-phase nature of the gas. In the centres of low-mass haloes (especially at smaller radii than shown), median temperatures tend to increase as densities drop. This is likely the result of stellar and/or AGN feedback heating some gas in the halo centres, increasing its temperature and volume. These large volumes for particles centred close to the halo centres may dominate the volume-weighted stacks. Indeed, in this regime, it seems gas at a few discrete temperatures sets these trends (including at $10^{7.5}$ K, the heating temperature for stellar feedback), and medians from a few randomly chosen individual galaxies do not show this trend.

The metallicities also tend to decline with radius, with larger differences in lower-mass haloes. Evidently, the metals are better mixed in high-mass haloes, likely because star formation and the accompanying metal enrichment tend to be quenched in these systems, while processes such as mergers and AGN feedback continue to mix the gas. The mass-weighted metallicities are higher than the volume-weighted ones in the inner parts of the halo, while in the outer halo and beyond R_{200c} , the differences depend on halo mass. For high-mass haloes, the median metallicity in the volume-filling phase drops sharply somewhat outside R_{200c} . However, the scatter in metallicity at large radii is very large, particularly at high masses.

Fig. 13 shows the corresponding ion-weighted temperature, density and metallicity profiles as a function of halo mass. The coloured, dotted lines in the temperature profiles show the T_{200c} at the median mass in each bin. The black, dotted lines indicate the CIE temperature range for each ion. Abrupt temperature changes are again a result of the median switching between different peaks in the temperature distribution of multiphase gas.

The ion-weighted temperature mostly follows the CIE temperature range (black dotted lines), rather than the T_{200c} range for that set of haloes (coloured dotted lines) within R_{200c} . Higher ion-weighted temperatures do occur, but in radial regions that contain relatively few ions. Ion-weighted temperatures below the CIE range mainly occur at radii $\gtrsim R_{200c}$, where ion-weighted hydrogen number densities reach the $\sim 10^{-5} \text{ cm}^{-3}$ regime where photo-ionization becomes important and lower-temperature gas can become highly ionized (Fig. 1). For O VI, ions at lower temperatures do persist at smaller radii, within the 90 per cent scatter of the ion-weighted temperature, and especially in lower-mass haloes.

The ion-weighted densities in the CGM reflect the halo’s physical properties: they follow the halo gas density distribution, and in particular, the volume-filling hot phase in cases where the mass- and volume-weighted gas distributions differ. They are however biased to the temperature ranges favoured by CIE and the metallicities are biased high compared to the mass- and volume-weighted values shown in Fig. 12.

These temperature and density effects may explain the ‘shoulders’ around R_{200c} in the absorption profiles at some

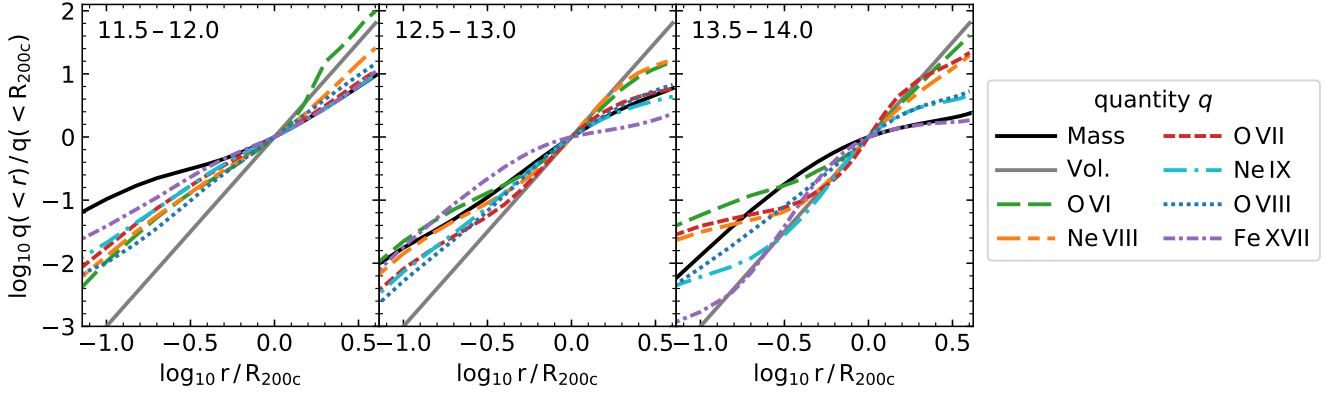


Figure 11. Average cumulative volume, gas mass, and ion mass 3-D profiles for the different ions. We show the average enclosed fraction of each quantity, normalized for each halo by the amount enclosed within R_{200c} . This shows that a large fraction of the ions is near R_{200c} . The different panels are for different M_{200c} ranges, shown in the top left corners in units $\log_{10} M_{200c} / M_{\odot}$. Since the trend with halo mass is weak, we only show three halo mass bins.

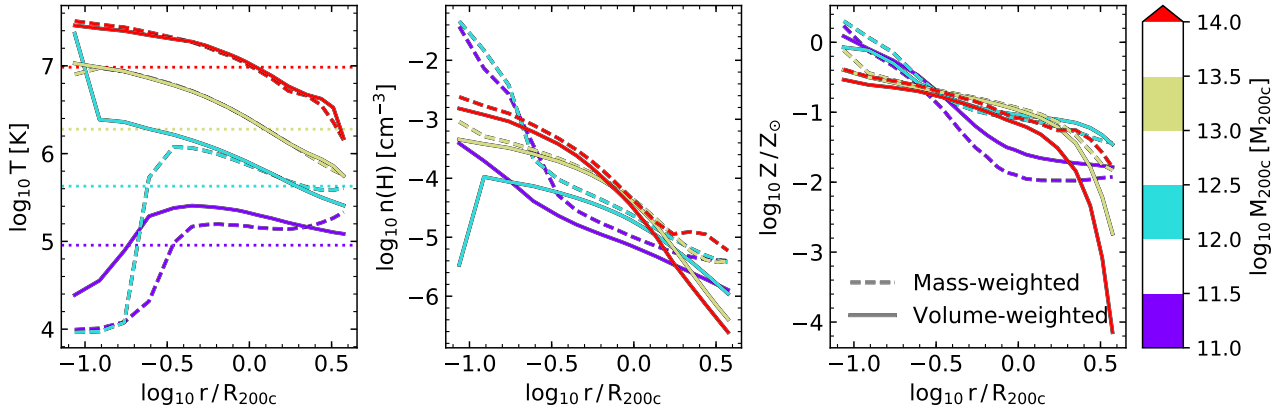


Figure 12. Mass-weighted (dashed) and volume-weighted (solid) median temperatures, densities, and metallicities of the halo gas. The radii are measured in three dimensions and normalized to R_{200c} for each halo before stacking. In the stacks, the values in each mass bin are first weighted by the indicated quantity for each halo, then the profiles for the haloes are weighted by the inverse of their mass or volume within R_{200c} before stacking. The dotted lines show T_{200c} (eq. 3) for the median halo mass in each bin, in colours matching the full range. The densities were calculated as mass densities and converted to hydrogen number densities assuming a primordial hydrogen mass fraction of 0.752. The metallicities are oxygen mass fractions ($\text{SMOOTHEELEMENTABUNDANCE}/\text{OXYGEN}$), normalized to a 0.00549 solar mass fraction (Allende Prieto et al. 2001). The neon and iron mass fractions (not shown) follow similar radial and halo mass trends, though the values differ somewhat. We show a subset of halo masses for legibility. The lowest-radius bin contains all mass/volume within $0.1 R_{200c}$.

halo masses seen in Fig. 6. This phenomenon occurs at halo masses around or above those for which T_{200c} matches the CIE peak for each ion. Since the temperature of the CGM decreases with radius, the ions will preferentially be present at larger radii in higher-mass haloes, where they form a ‘shell’, which produces large column densities at projected radii close to the shell radius. This is visible in Fig. 11, where lower ions in higher-mass halos have S-shaped cumulative ion mass distributions, with relatively little ion mass in the too-hot inner CGM.

However, around R_{200c} , as the halo-centric radius increases, the effect of the declining gas temperature is countered by photo-ionization of the cold phase, which also starts

to become important around R_{200c} . This drives the preferred temperatures of the ions down with radius, along with the gas temperature. The ‘shoulders’ are strong in Fe XVII and Ne IX profiles; these ions have the highest ionization energies (Table 1) and are photo-ionized at lower densities (Fig. 1) than the others.

The sharp drops in the absorption profiles at large radii in Fig. 6 may also be explained by these halo properties: the gas density drops outside R_{200c} , and more sharply for higher halo masses. Similarly, the gas metallicity drops rapidly around these radii in the high-mass haloes. The differences between the ions seem to be consistent with the more easily photo-ionized ones producing more absorption in the cooler,

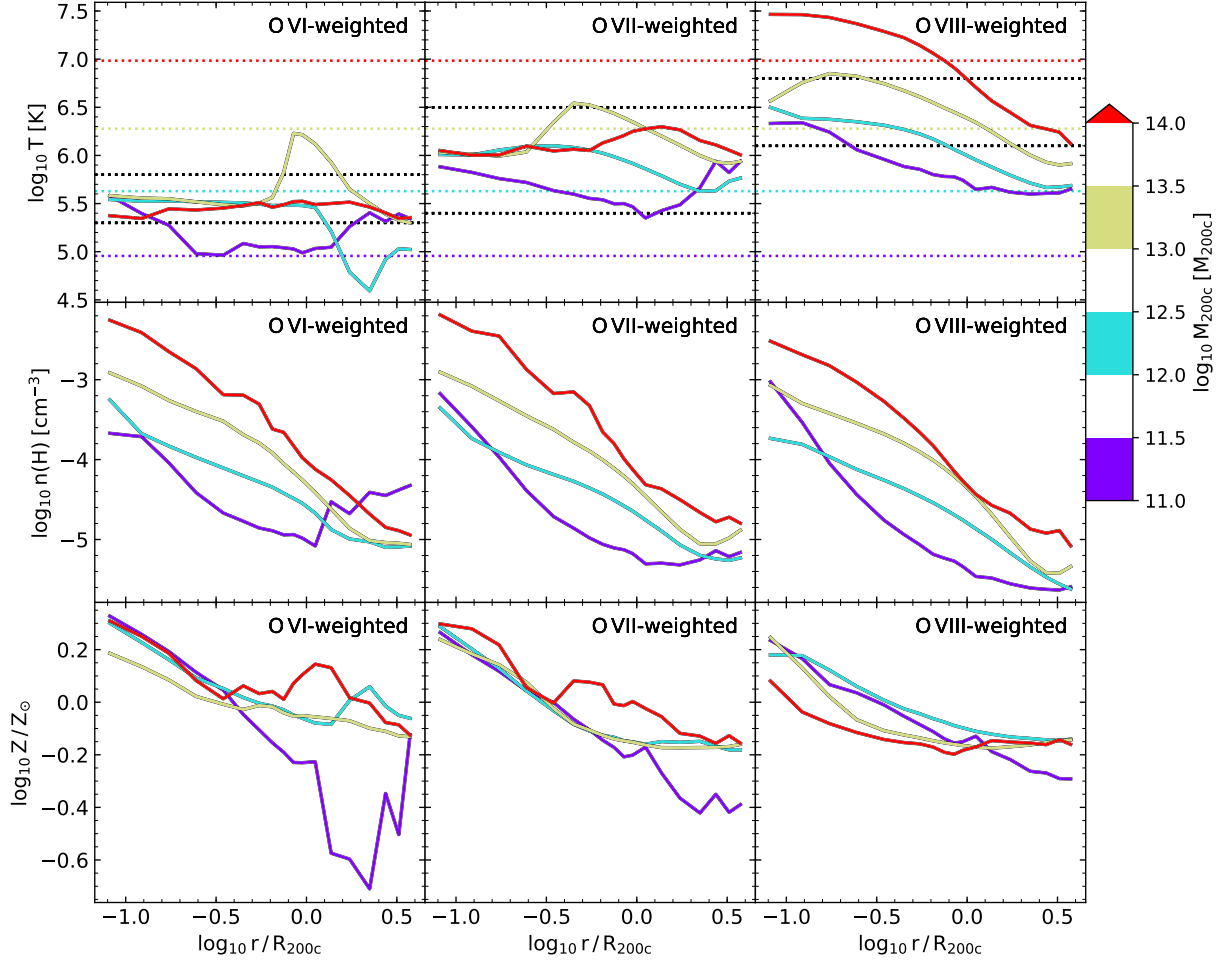


Figure 13. Ion-weighted median temperatures, densities, and metallicities of the halo gas for O VI–VIII. The radii are measured in three dimensions and normalized to R_{200c} for each halo before stacking. In the stacks, the ion-weighted profile for each halo is weighted by the inverse of ion mass within R_{200c} . The dotted, coloured lines show T_{200c} (eq. 3) for the median halo mass in each bin, while the black dotted lines show the CIE temperature range for each ion (Table 1). The densities were calculated as mass densities and converted to hydrogen number densities assuming a primordial hydrogen mass fraction of 0.752. The metallicities are oxygen mass fractions ($\text{SMOOTHEELEMENTABUNDANCE}/\text{OXYGEN}$), normalized to the 0.00549 solar mass fraction of Allende Prieto et al. (2001). The ion temperatures are mostly set by CIE, while their densities roughly follow the volume-weighted density profile (i.e., the hot gas profile, Fig. 12). The metallicities are biased high compared to Fig. 12.

lower-density gas around R_{200c} . However, the way the CIE temperature range lines up with gas temperatures depends on both the ion and the halo mass, so ion and mass trends are difficult to disentangle.

Though Fe XVII seems like an outlier in Fig. 11, in that it is more concentrated in halo centres than the (total) gas mass, this does fit into these trends: the outskirts of most haloes at the masses we consider are simply too cool for this ion. However, in $M_{200c} > 10^{14} M_{\odot}$ haloes, which have T_{200c} above the preferred range of Fe XVII, the absorption does extend out to R_{200c} , albeit at lower column densities.

We note that the sharp drops in mass- and volume-weighted median metallicity are not in contradiction with the flat ion-weighted metallicities outside R_{200c} : there is very large scatter in the metallicity at large radii, and metal

ions will preferentially exist in whatever metal-enriched gas is present.

3.6 Connection to the central galaxy

In this section, we show radial profiles that can be more readily compared to observations: absorption around galaxies of a given stellar mass, as a function of projected distance to the galaxy centre of mass. Unlike before, we obtain the median and scatter in column density in bins of physical impact parameter. We only consider central galaxies here. The profiles are shown in Fig. 15.

We use bins spaced by 0.5 dex in stellar mass throughout this section. However, we do not use a separate bin for $M_{\star} = 10^{11.5} - 10^{11.7} M_{\odot}$, since this bin would only contain six galaxies. Instead, we group all $M_{\star} > 10^{11} M_{\odot}$ galaxies

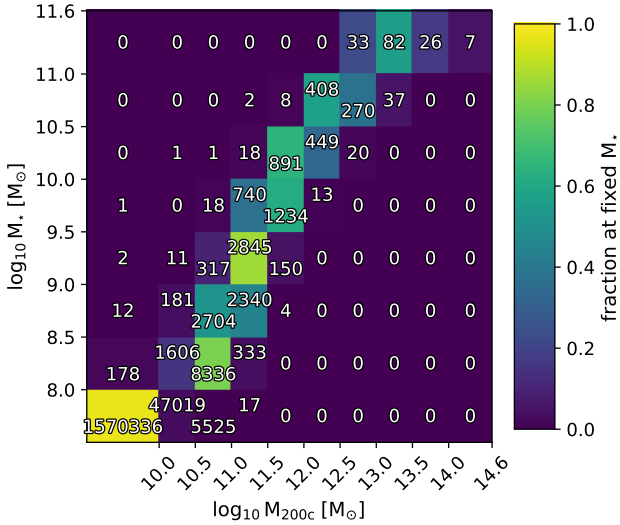


Figure 14. The EAGLE M_\star - M_{200c} relation for central galaxies shown as a confusion matrix, demonstrating how our M_\star and M_{200c} bins compare. The number of central galaxies in each M_\star , M_{200c} bin is shown. The lowest-mass bins have no lower limit, and include galaxies and haloes that are unresolved in the simulation. The colours show what fraction of galaxies in each M_\star bin are in haloes in different M_{200c} bins.

into one bin. We use at most 1000 galaxies (randomly selected) for the profiles for each M_\star bin, which is relevant for galaxies with $M_\star < 10^{10.5} M_\odot$.

Fig. 14 shows the stellar-mass-halo-mass relation for EAGLE central galaxies as a ‘confusion matrix’. It shows how the stellar mass bins we use in this section map onto the halo mass bins used in the rest of the paper. According to Schaye et al. (2015), the galaxy stellar mass function is converged with resolution down to stellar masses $M_\star \approx 2 \times 10^8 M_\odot$, though for other properties, such as star formation rates, the lower limit is $\sim 10^9 M_\odot$ or somewhat more massive. In the lowest halo mass bin we considered ($M_{200c} = 10^{11-11.5} M_\odot$), we do find a substantial contribution from $M_\star < 10^9 M_\odot$ galaxies, but most central galaxies in this halo mass bin have $M_\star > 2 \times 10^8 M_\odot$. Fig. 14 also shows that the highest three halo mass bins will have little impact outside the largest stellar mass bin, and the very largest halo mass bin contains too few galaxies to contribute significantly for any stellar mass.

Fig. 15 shows the same main trends of column density with M_\star in physical distance units as Fig. 6 showed for normalized distance and halo mass. However, for O VIII, Ne IX, and Fe XVIII, the fact that the highest-stellar-mass bin contains mostly $M_{200c} < 10^{13.5} M_\odot$ haloes means we do not see a decrease in column density towards the highest stellar masses. The overall correspondence implies that, with sufficiently sensitive instruments and large enough sample sizes, the column density trends with halo mass should be observable.

Note that the innermost parts of these profiles ($r_\perp \ll 10$ pkpc) might be less reliable, where they probe the central galaxy or gas close to it. Wijers et al. (2019) found that including or excluding star-forming gas altogether has very little effect on the CDDFs of O VII and O VIII. Indeed, in

Table 5. Threshold column densities ($\log_{10} N$ [cm $^{-2}$]) used for covering fractions for the different ions we show in Figs. 16 and 17. The EW cited in the top line of the table is an observer-frame (redshifted) value. It was converted into column densities using the lines from Table 2 at $z = 0.1$, and the best-fit b parameters from Table 3. The sources for the data are described in the text.

	O VI	Ne VIII	O VII	Ne IX	O VIII	Fe XVII
EW = 0.18 eV			15.4	15.4	15.6	14.8
HST-COS	13.5	13.5				
CDDF break	14.3	13.7	16.0	15.3	16.0	15.0

making the column density maps, we assumed all this gas had a temperature of 10^4 K, too cool for these ions at these high densities (Fig. 1). However, in reality, a hot phase in the ISM may contain such ions. On the other hand, in EAGLE, the hot, low-density gas we noticed in halo centres in §3.5, which may have been directly heated by star formation or AGN feedback, might cause absorption that is sensitive to the adopted subgrid heating temperatures associated with these processes.

Next, we look into covering fractions. We list the limiting column densities we use for this in Table 5. We use two column density thresholds for each ion. Fig. 16 uses the approximate locations of the breaks in the CDDFs (Fig. 2). For a number of ions, the absorption lines we analyse here (Table 2) (start to) become saturated at these column densities (Fig. 3). For unresolved X-ray lines, these covering fractions might therefore be difficult to measure observationally as long as the widths of the absorption components remain unresolved, which is expected even for the Athena X-IFU (Wijers et al. 2019, fig. 4).

Fig. 17 uses column density thresholds which correspond roughly to the detection limits of current, blind (UV) and upcoming (X-ray) surveys. For the X-ray ions, we use the minimum observable EW for the X-IFU on the planned Athena mission, shown in Fig. 17. Here, weak lines around 1 keV should be detectable at 5σ significance at observer-frame EWs of 0.18 eV. This is for 50 ks exposure times and a quasar background source with a 2–10 keV flux of 10^{-11} erg cm $^{-2}$ s $^{-1}$ and a photon spectral index $\Gamma = 1.8$ (Lumb et al. 2017). Blind detections of pairs of O VII and O VIII absorption lines should be possible at lower EWs than this, at least against bright Gamma-ray burst background sources (Walsh et al. 2020).

For the FUV ions, we choose column densities based on what is currently observed with the Hubble Space Telescope’s Cosmic Origins Spectrograph (HST-COS). We base estimates on observed column densities and upper limits, and column densities used for covering fractions by observers. We use the data of Tumlinson et al. (2011) and Prochaska et al. (2011) for O VI, and of Burchett et al. (2019) and Meiring et al. (2013) for Ne VIII. Note that our limits are for $z = 0.1$ for consistency, but the EUV line we discuss for Ne VIII is only observable at higher redshifts. We explore the redshift evolution of the absorption in Appendix C.

In Fig. 16, we see that the covering fractions above the CDDF break typically peak close to galaxies. However, the relatively small cross-section of these central regions means that absorption above the break in the CDDF for blind surveys is dominated by regions outside the inner 30 pkpc

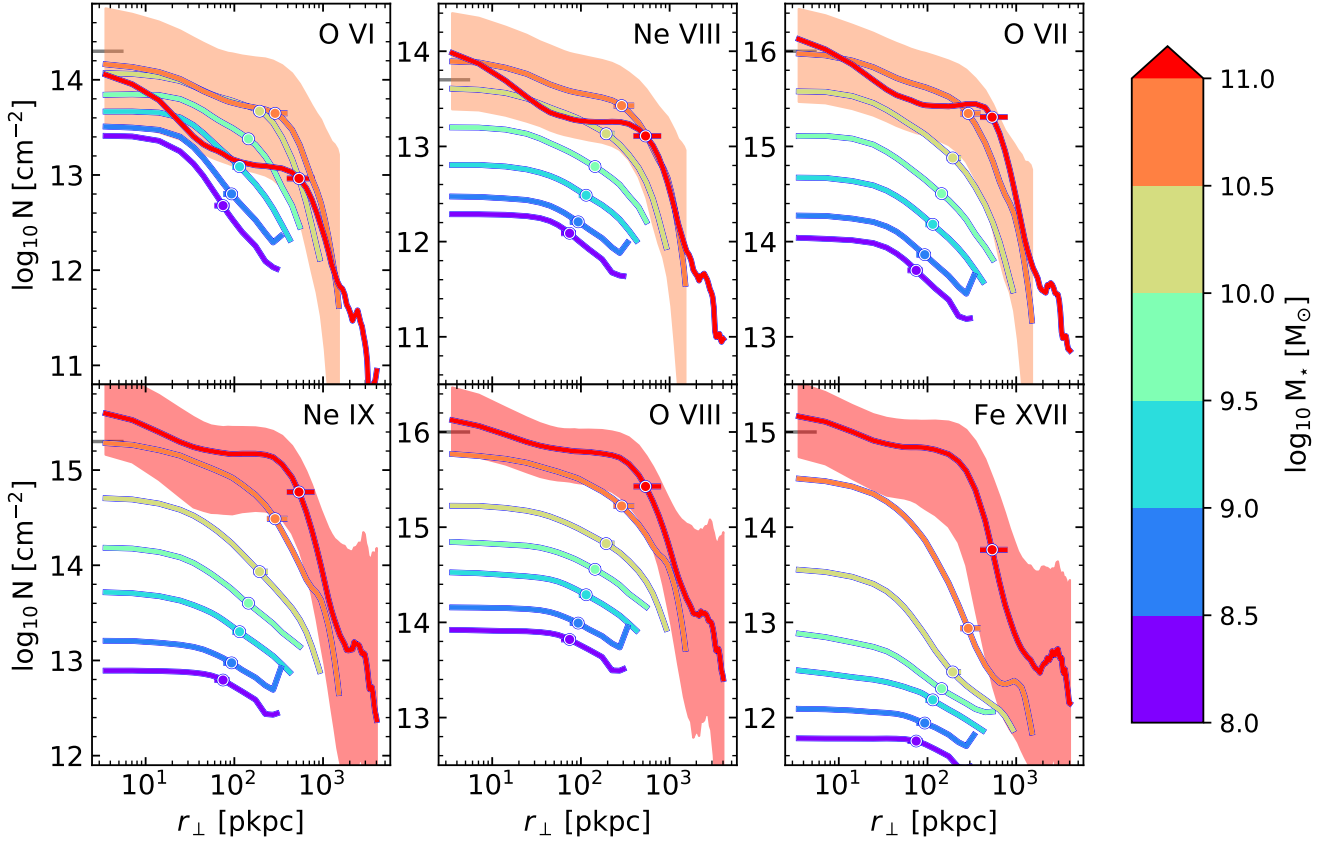


Figure 15. Median column density as a function of impact parameter (physical distance) and stellar mass of the central galaxy. Different panels are for different ions. Long ticks on the y-axes (left) indicate approximately where the breaks in the CDDFs occur (Fig. 2). The profiles extend out to $3R_{200c}$ of the 99th percentile of the M_{200c} distribution of each M_\star bin (see Fig. 14). Points on each curve mark the median virial radius in each M_\star bin, and horizontal lines show the central 80 per cent of virial radii in those bins.

around galaxies. We determined this from the covering fraction profiles at different M_\star , and the total CDDFs for the ions. We compared different sets of absorbers. The first set are the absorbers in the central regions. These are absorbers in the same 6.25 cMpc slice of the simulation, with impact parameters $r_\perp < 30$ pkpc (< 30 pkpc absorbers). The second set is similar, but contains absorbers with $r_\perp \lesssim R_{200c}$. In each stellar mass bin, we use the median R_{200c} of the parent haloes to define the edge. We estimate the number of absorbers above the column density breaks in the two r_\perp ranges from the covering fraction profiles.

The < 30 pkpc absorbers contain $\lesssim 10$ per cent of the absorption above the CDDF break in the $\lesssim R_{200c}$ sample, at least in M_\star bins responsible for > 10 per cent of the total absorption above the CDDF breaks. For M_\star bins responsible for less of the total absorption, the < 30 pkpc absorbers make up $\lesssim 33$ per cent of the $\lesssim R_{200c}$ absorbers (with one exception of 42 per cent: Fe XVII around $M_\star = 10^{10} - 10^{10.5} M_\odot$ galaxies). Looking back to Fig. 15, this also means that absorption above the CDDF break is indeed dominated by scatter in column densities around galaxies at larger radii, rather than typical absorption where column densities are highest.

Fig. 17 gives a sense of observing prospects: for O VI and Ne VIII, these are more optimistic (but achievable) minimum

column densities for HST-COS, reflecting currently possible observations. Many of these have also been done. We discuss some EAGLE data comparisons in §4. For $\sim L_\star$ galaxies, O VI should be widely observable according to EAGLE, and Ne VIII should be widely observed in the L_\star -group mass range. The Burchett et al. (2019) observations (at $z \approx 0.5 - 1.1$) report Ne VIII absorbers and upper limits around galaxies in a wide mass range ($M_\star \sim 10^9 - 10^{11} M_\odot$), which covers a large range in covering fractions in our predictions and makes a direct comparison to our figures difficult.

For the X-ray lines, Fig. 17 shows estimated detection limits for the Athena X-IFU. These estimates are on the rough side for Fe XVII and Ne IX, since the oxygen lines have been the main focus of WHIM and hot CGM detection plans. These lines are at different energies, so the energy-dependence of the sensitivity of the instrument and the spectrum of the background source and Galactic absorption, mean that 0.18 eV might not be an appropriate minimum EW for Ne IX and Fe XVII. Besides that, the relation between column density and EW has enough scatter above the minimum observable EW that it does not quite translate into a unique minimum column density, but it is an acceptable approximation in this regime (Wijers et al. 2019, appendix B).

Detection prospects for CGM out to large distances (close to R_{200c}) look good for O VII and O VIII, and in a nar-

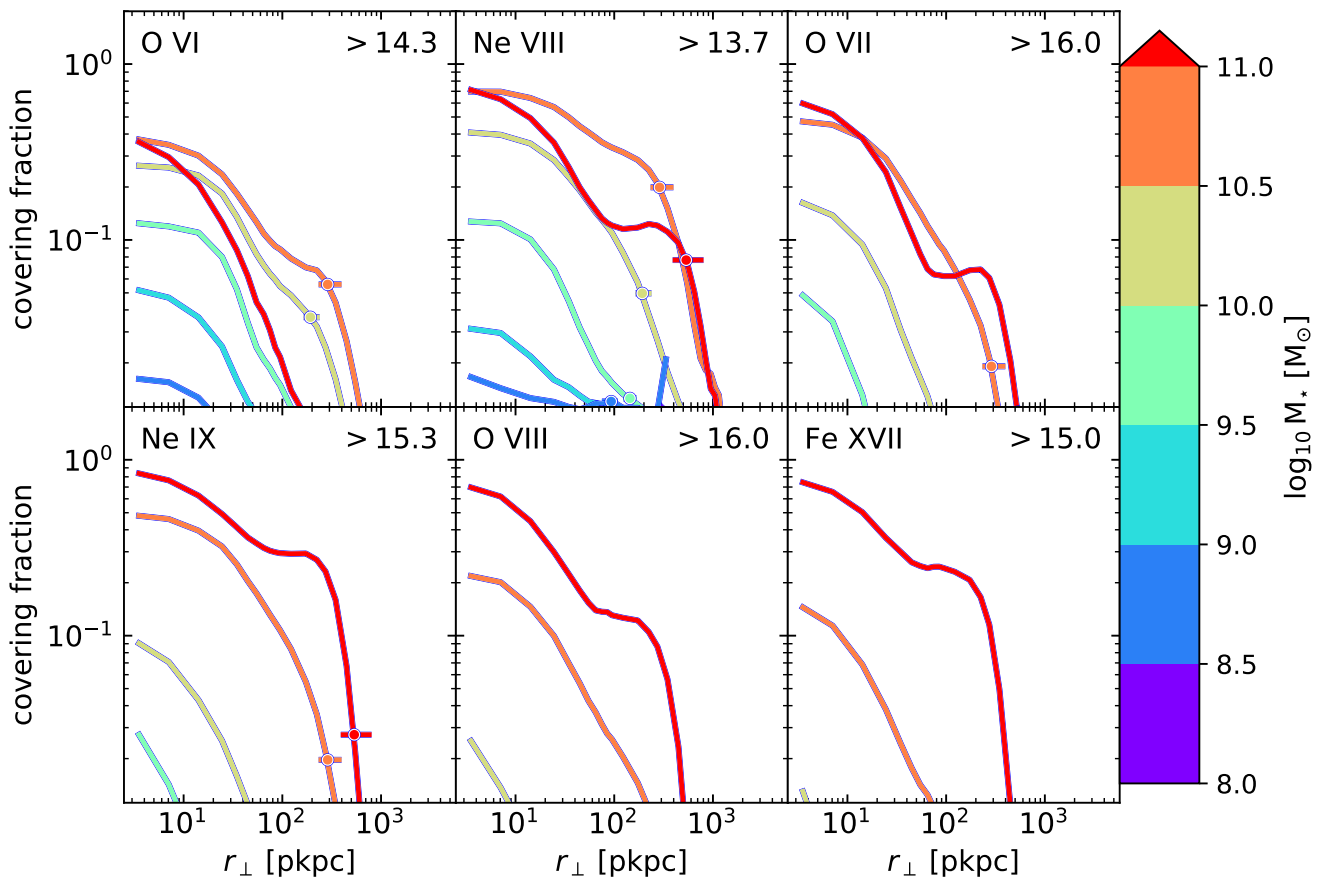


Figure 16. Covering fractions around central galaxies of different stellar masses as a function of physical impact parameter. The covering fraction is the fraction of sightlines with column densities larger than a threshold value at each impact parameter. The threshold column densities, in $\log_{10} \text{ cm}^{-2}$ units, are shown in the panels. These covering fractions are for column densities equal to the respective CDDF breaks. Points on each curve mark the median virial radius in each M_* bin, and horizontal lines show the central 80 per cent of virial radii in those bins. (Some are outside the range of the plot.)

rower mass range, for Fe XVII. Ne IX might, however, prove more difficult to detect at larger impact parameters. However, these limits are for blind detections, and hence conservative for targeted observations. It might thus be possible to find Ne IX counterparts to absorbers in e.g., O VIII, or to detect weaker lines by searching at known galaxy redshifts. For most of the X-ray ions, the detection thresholds are not very far from the CDDF breaks, so small changes in sensitivity could make large differences for detection prospects, as the difference between Figs. 16 and 17 shows.

We also make predictions for the proposed Arcus (Smith et al. 2016; Brenneman et al. 2016) mission, and the X-ray Grating Spectrometer (XGS) on the proposed Lynx mission (The Lynx Team 2018). As with the Athena X-IFU, we estimate the minimum detectable column density from the minimum detectable EW and the b -parameters from Table 3, assuming a single Voigt profile (or a doublet, for O VIII). Since these minima depend not just on the instrument, but on the observations (e.g., exposure time, background source flux and spectrum), we take the minimum EWs from the instrument science requirements, which assume a planned observing campaign as well as instrument properties. These are observer-frame minima, which we convert to rest-frame

minimum EWs assuming $z = 0.1$, the redshift we assume throughout this work.

For Arcus, that means we assume a minimum detectable EW of 4 m\AA (for 5σ detections). This is based on bright AGN background sources, which were selected to have a high flux between 0.5 and 2 keV (Brenneman et al. 2016), and exposure times $< 500 \text{ ks}$ (Smith et al. 2016). At least 40 blazars matching the brightness requirements are known (Smith et al. 2016). These estimates are based only on O VII and O VIII (and C VI), so this minimum EW may not apply to the Ne IX and Fe XVII lines at smaller wavelengths. Note that Arcus not only aims to find weaker absorption lines than the Athena X-IFU, it is also meant to characterise them in more detail using its higher spectral resolution. Arcus has a $\approx 6\text{--}8\times$ higher spectral resolution than Athena at the wavelengths of O VII and O VIII at $z = 0.1$, which is sufficient ($\approx 120\text{--}150 \text{ km s}^{-1}$, Smith et al. 2016) to determine if absorbers are associated with L_* galaxy haloes that have typical virial velocities of $150\text{--}300 \text{ km s}^{-1}$, while the Athena X-IFU’s resolution ($\approx 900\text{--}1000 \text{ km s}^{-1}$, Barret et al. 2018) would be insufficient to determine if absorbers belong to individual galactic halos.

For the Lynx XGS, the requirement is a detectable EW

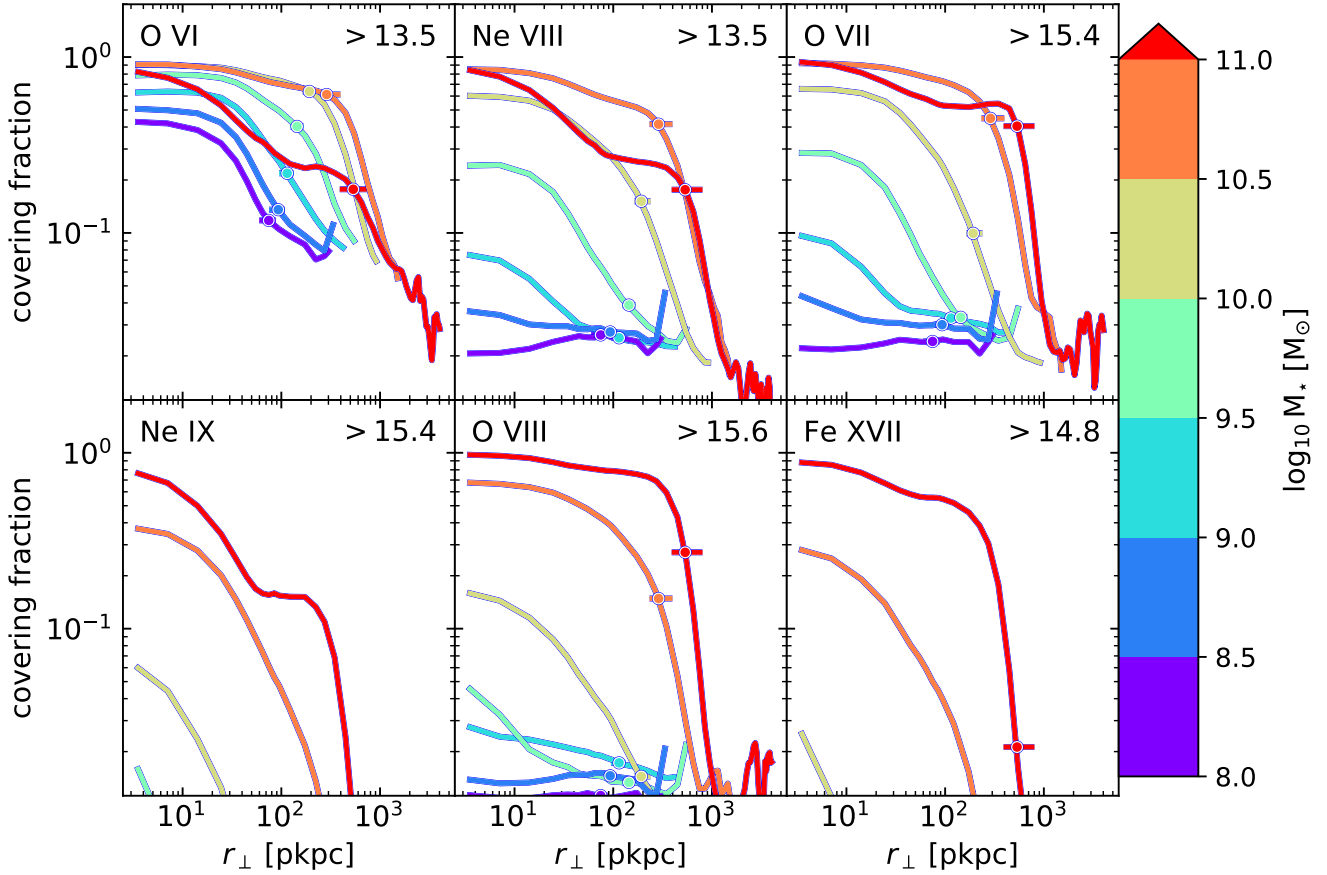


Figure 17. Covering fractions around central galaxies of different stellar masses as a function of physical impact parameter. The covering fraction is the fraction of sightlines with column densities larger than a threshold value at each impact parameter. The threshold column densities, in $\log_{10} \text{ cm}^{-2}$ units, are shown in the panels. Points on each curve mark the median virial radius in each M_\star bin, and horizontal lines show the central 80 per cent of virial radii in those bins. (Some are outside the range of the plot.) These covering fractions are for optimistic HST-COS detection limits (O VI, Ne VIII) and estimated Athena X-IFU limits (X-ray lines). The Athena limits are for observer-frame EWs of 0.18 eV (0.16 eV rest-frame). That is the expected minimum for 5σ detections, assuming 50 ks exposure times and a quasar background source with a 2–10 keV flux of $10^{-11} \text{ erg cm}^{-2} \text{ s}^{-1}$ and a photon spectral index $\Gamma = 1.8$ (Lumb et al. 2017).

of 1 mÅ for O VII and O VIII (The Lynx Team 2018). This applies to 80 bright AGN background sources in a 5 Ms survey, focussed on detecting the CGM of $\sim L_\star$ galaxies in absorption.

We therefore limit this discussion to O VII and O VIII. The minimum EWs for Arcus translate to column densities of $10^{15.3}$ and $10^{15.6} \text{ cm}^{-2}$ for O VII and O VIII, respectively. For Lynx, the values are, respectively, $10^{14.6}$ and $10^{14.9} \text{ cm}^{-2}$. Using the median column density profiles from Fig. 15, we find the radii where the covering fractions at the detection limits for the different instruments reach 0.5. Note that this is the covering fraction in annuli, not circles, of these radii. These are shown in Table 6.

This confirms that with the Athena X-IFU, we should be able to find O VII and O VIII absorption out to close to R_{200c} for $M_\star > 10^{10.5} M_\odot$ galaxies. Arcus performs similarly; we note that compared to the Athena X-IFU, it does have a much higher spectral resolution for soft X-rays. Lynx should be sensitive to much weaker absorption lines, and should therefore be able to find absorption systems beyond the virial radii of $M_\star > 10^{10.5} M_\odot$ galaxies, and roughly up

Table 6. Impact parameters r_\perp / pkpc, rounded to 10 pkpc, where the covering fraction $f(> N) = 0.5$ for different ions, galaxy masses, and column density limits. The column density limits (indicated in the third row in $\log_{10} \text{ cm}^{-2}$) are calculated for the different ions and instruments as explained in the text. We estimate the limits for the Athena X-IFU (Athena), Arcus, and the Lynx XGS (Lynx). A dash (‘-’) means that the covering fraction is below 0.5 at all radii.

M_\star $\log_{10} M_\odot$	O VII			O VIII		
	Athena 15.4	Arcus 15.3	Lynx 14.6	Athena 15.6	Arcus 15.6	Lynx 14.9
10.0–10.5	30	50	340	-	-	140
10.5–11.0	260	310	680	50	50	560
11.0–11.7	460	540	930	410	410	910

to the virial radii of $M_\star = 10^{10}–10^{10.5} M_\odot$ galaxies. Indeed, one of the mission goals is to characterise the CGM of $\sim L_\star$ galaxies using these absorption lines (The Lynx Team 2018).

4 DISCUSSION

All of the predictions reported in the previous section are based on the EAGLE simulation. EAGLE reproduces a number of galaxy and diffuse gas properties, to differing degrees. At the highest halo masses we study ($M_{500c} \gtrsim 10^{13.5} M_{\odot}$), there are observations available to compare hot gas properties of the ICM to. At lower masses, the gas properties are less well-constrained. Schaye et al. (2015) showed that EAGLE matches the relation between M_{500c} (X-ray) and I-band luminosity $\sim M_{\star}$ well, but overestimates ICM gas fractions at fixed halo mass (from X-ray measurements) and soft X-ray luminosities at fixed X-ray spectroscopic temperature above 1 keV. Overall, the higher gas fractions mean we might overestimate column densities from these simulations.

Other authors have studied UV absorption in simulations, particularly CDDFs and absorption around L_{\star} to group-mass haloes. Rahmati et al. (2016, EAGLE) found that the O VI CDDF is somewhat underpredicted at the high column density end, though uncertainties in the observations and oxygen yields may mean the difference is not severe. They found the cosmic Ne VIII density agreed with that measured by Meiring et al. (2013), though the measurements and comparisons are somewhat uncertain.

Oppenheimer et al. (2016) made a comparison of the absorption in $\sim L_{\star}$ to group-mass halo zoom-in simulations using the EAGLE simulation code to COS-Halos (Tumlinson et al. 2011) and found similar trends with star formation rates, but overall somewhat too low O IV column densities in $\sim L_{\star}$ haloes. Oppenheimer et al. (2018) found that those higher O VI columns could be achieved though ionization by radiation from flickering AGN, in combination with non-equilibrium ionisation, but that the CDDF discrepancy is likely not resolvable this way. This radiation and non-equilibrium ionisation also affects other ions. The effect on O VII column densities is, however, small: they decrease by $\lesssim 0.1$ dex.

Nelson et al. (2018) compared their data to COS-Haloes survey results for O VI (Tumlinson et al. 2011), complemented by galaxy data, and to the eCGM survey data (Johnson et al. 2015), and found generally good agreement. For their calibrated TNG-100-1 volume, the O VI CDDF might be too large at high column densities.

For O VI, there are long-standing difficulties in modelling observed absorbers (in combination with lower ions) due to the uncertain ionization mechanism (e.g., Werk et al. 2016). We find that, in EAGLE, the O VI is mostly collisionally ionized in the inner regions, but photo-ionized at $\gtrsim R_{200c}$, and that photo-ionized O VI is present in the inner regions of lower-mass haloes. In IllustrisTNG CIE is most important mechanism in the CGM (Nelson et al. 2018), as in EAGLE, assuming ionization equilibrium. However, the results of Oppenheimer et al. (2018) demonstrate that, at least for the CGM of $\sim L_{\star}$ galaxies, such equilibrium assumptions may underestimate the effect of photo-ionization. They used non-equilibrium ionization, and a flickering AGN as an additional ionization source, in zoom simulations otherwise using the EAGLE code and physics. In NIHAO and VELA zoom simulations, Roca-Fàbrega et al. (2019) found a roughly equal mix of collisionally and photo-ionized O VI in $z = 0$, $M_{200c} = 10^{11} - 10^{12.6} M_{\odot}$ haloes. Overall, this sup-

ports the picture that observed O VI does not have one single origin.

Nelson et al. (2018) also looked into O VII and O VIII absorption in the CGM. They found column densities that peak at similar masses as we find, and ion fraction trends with halo mass similar to ours except at the lowest masses we examine, though they measure the fractions in a somewhat different gas selection.

An issue that has come up more recently is the effect of resolution on cool gas in the CGM. Though radiative (metal-line) cooling is now standard in cosmological and zoom-in galaxy simulations, a characteristic length scale associated with such cooling is not always resolved: the cooling length, equal to the product of the cooling time and sound speed in the gas, which sets a typical scale for the cooled gas clouds (e.g., McCourt et al. 2018).

Recently, a number of groups have run simulations zooming in on single L_{\star} haloes, but with higher resolution in the diffuse CGM than is reached in cosmological volumes. Generally, the global properties of the haloes, such as galaxy stellar masses and CGM mass, and the absorption by high ions, are insensitive to this resolution, but there may be effects on e.g., high-column-density H I (van de Voort et al. 2019; Peeples et al. 2019; Hummels et al. 2019). However, the smallest cooling lengths expected in the CGM are, still unresolved (Peeples et al. 2019), which may lead to an underestimate of the cool gas in simulations (e.g., Hummels et al. 2019).

5 CONCLUSIONS

Using the EAGLE simulation, we investigate the contents and properties of the CGM, and how they are probed by O VI (FUV), Ne VIII (EUV) and O VII, O VIII, Ne IX, and Fe XVII (X-ray) line absorption at $z = 0.1$. With future X-ray instruments like the Athena X-IFU, Arcus, and the Lynx XGS, we expect that some of these absorption lines can be used to study the hot CGM. The mass of this CGM phase in $\sim L_{\star}$ and group-mass haloes is largely unconstrained by current observations, and differs in different cosmological simulations. Determining the mass and metal content of the hot CGM will therefore provide important constraints for our understanding of structure and galaxy formation.

We find that the CGM is the largest baryonic mass component in EAGLE haloes at all masses we investigate ($M_{200c} > 10^{11} M_{\odot}$), and is particularly dominant at $M_{200c} \gtrsim 10^{13} M_{\odot}$ (Fig. 7). The CGM also contains more oxygen than the ISM for all halo masses, though differences are small at $M_{200c} \lesssim 10^{12} M_{\odot}$. However, up to $M_{200c} \approx 10^{13} M_{\odot}$, stars contain most of the oxygen ejected by earlier stellar generations that remains within R_{200c} (Fig. 8). The ions we study mainly trace CGM gas at $10^{5.5} - 10^7$ K, which constitutes a large fraction of the CGM mass in $M_{200c} \approx 10^{12} - 10^{13.5} M_{\odot}$ haloes (Fig. 7). Indeed, these are the haloes where these ions have the largest column densities (Fig. 6).

The CDDFs for these ions have shallow slopes at lower column densities and a ‘tail’ with a steep slope at high column densities (Fig. 2). For the X-ray ions, the high-column-density tail of the CDDF is produced mostly by CGM gas (Fig. 5): 70–80 per cent has an impact parameter $r_{\perp} < R_{200c}$

for a halo with $M_{200c} > 10^{11} M_{\odot}$. These very high column densities are above the CGM median in these haloes, and are produced mainly by haloes in a limited mass range (Fig. 6). Although median column densities are higher in halo centres, these central regions do not dominate this high column density absorption in blind surveys.

The mass ranges for which median column densities are highest are in line with simple predictions comparing the virial temperature with the temperature where the ion fraction peaks in CIE (Fig. 1). This is because these ions mainly trace gas at temperatures around the CIE peak in the volume-filling phase of the CGM (Figs. 12 and 13). In addition, the metal-line absorption is biased towards high-metallicity gas. In the inner CGM, these ions are all mainly collisionally ionized (although some O VI is photo-ionized), but close to R_{200c} , photo-ionization becomes relevant. This combination of multi-phase gas, the temperature gradient in the volume-filling phase, and different ionization mechanisms means that the haloes exhibit a larger diversity of ions than the single-temperature CIE model alone would predict.

We note an interesting feature in the column density profiles: the column densities do not always decrease as the halo-centric impact parameter increases. This occurs in haloes with T_{200c} above the CIE peak temperature of the absorbing ion, where we find peaks or ‘shoulders’ in the column density profiles (Fig. 6). This occurs because the temperature of the volume-filling phase declines towards the outskirts of the halo (Fig. 12), causing the ion fraction to be larger there. Despite the decline of gas density with radius, this leads to a ‘shell’ around the galaxy where most of the metals in a particular ionization state are found (Fig. 11). In projection, depending on the strength of the shell feature, this leads to a peak or flattening of the column density as a function of halo-centric radius, typically around R_{200c} .

For most of these ions, column densities remain large out to $\sim R_{200c}$ in haloes of the right mass (Fig. 6), and O VII and O VIII should be detectable with Athena that far out around $M_{\star} > 10^{10.5} M_{\odot}$ galaxies (Fig. 17). However, Fe XVII absorption is more centrally concentrated, and more confined to haloes than the other ions in general (Fig. 4). Ne IX and Fe XVII might prove more difficult to find in the CGM with Athena, because the (roughly estimated) minimum observable column densities for these ions are close to, or in, the high-column-density tail of the CDDF. At column densities expected to be detectable with the Athena X-IFU, some of the absorption lines will be saturated. However, the saturation is less severe than thermal line broadening would predict for the temperatures where the CIE ionization fractions peak (Fig. 3). Our set of ions is mostly suited to probe haloes of $M_{200c} \sim 10^{12} - 10^{13.5} M_{\odot}$, though O VI, and Ne VIII at $z = 0.5$, also probe lower halo masses, and Fe XVII also probes somewhat hotter haloes.

ACKNOWLEDGEMENTS

We would like to thank Rob Crain and Fabrizio Nicastro for their involvement in the beginning of the project. NAW and BDO would like to thank Akos Bogdan, Ralph Kraft, Randall Smith, and Alexey Vikhlinin for useful discussions. We would additionally like to thank John Helly for programs we used to access EAGLE data (READ_EAGLE),

and Volker Springel for the original version of the code we use to project particles onto a grid (HSMMLANDPROJECT). Ali Rahmati helped NAW test the code we use to make projections and helped set up SPECWIZARD. We used the NUMPY (Oliphant 2006), SCIPY (Jones et al. 2001), H5PY (Collette 2013), and MATPLOTLIB (Hunter 2007) PYTHON libraries, and the IPYTHON (Pérez & Granger 2007) command-line interface. This paper is supported by the European Union’s Horizon 2020 research and innovation programme under grant agreement No 871158, project AHEAD2020. This work used the DiRAC@Durham facility managed by the Institute for Computational Cosmology on behalf of the STFC DiRAC HPC Facility (www.dirac.ac.uk). The equipment was funded by BEIS capital funding via STFC capital grants ST/K00042X/1, ST/P002293/1, ST/R002371/1 and ST/S002502/1, Durham University and STFC operations grant ST/R000832/1. DiRAC is part of the National e-Infrastructure.

REFERENCES

- Abazajian K. N., et al., 2016, arXiv e-prints, [p. arXiv:1610.02743](https://arxiv.org/abs/1610.02743)
Ahoranta J., et al., 2019, arXiv e-prints, [p. arXiv:1912.06659](https://arxiv.org/abs/1912.06659)
Allende Prieto C., Lambert D. L., Asplund M., 2001, *ApJ*, **556**, L63
Anderson M. E., Bregman J. N., Dai X., 2013, *ApJ*, **762**, 106
Anderson M. E., Churazov E., Bregman J. N., 2016, *MNRAS*, **455**, 227
Barnes D. J., et al., 2017, *MNRAS*, **471**, 1088
Barret D., et al., 2016, in Society of Photo-Optical Instrumentation Engineers (SPIE) Conference Series. p. 99052F ([arXiv:1608.08105](https://arxiv.org/abs/1608.08105)), doi:10.1117/12.2232432
Barret D., et al., 2018, in Society of Photo-Optical Instrumentation Engineers (SPIE) Conference Series. p. 106991G ([arXiv:1807.06092](https://arxiv.org/abs/1807.06092)), doi:10.1117/12.2312409
Bernitt S., et al., 2012, *Nature*, **492**, 225
Bertone S., Schaye J., Dalla Vecchia C., Booth C. M., Theuns T., Wiersma R. P. C., 2010a, *MNRAS*, **407**, 544
Bertone S., Schaye J., Booth C. M., Dalla Vecchia C., Theuns T., Wiersma R. P. C., 2010b, *MNRAS*, **408**, 1120
Bogdán Á., et al., 2015, *ApJ*, **804**, 72
Bonamente M., Nevalainen J., Tilton E., Liivamägi J., Tempel E., Heinämäki P., Fang T., 2016, *MNRAS*, **457**, 4236
Booth C. M., Schaye J., 2009, *MNRAS*, **398**, 53
Branchini E., et al., 2009, *ApJ*, **697**, 328
Bregman J. N., Lloyd-Davies E. J., 2007, *ApJ*, **669**, 990
Brenneman L. W., et al., 2016, in Space Telescopes and Instrumentation 2016: Ultraviolet to Gamma Ray. p. 99054P, doi:10.1117/12.2231193
Burchett J. N., et al., 2019, *ApJ*, **877**, L20
Carswell B., Schaye J., Kim T.-S., 2002, *The Astrophysical Journal*, **578**, 43
Cen R., Fang T., 2006, *ApJ*, **650**, 573
Cen R., Ostriker J. P., 1999, *ApJ*, **514**, 1
Chen X., Weinberg D. H., Katz N., Davé R., 2003, *ApJ*, **594**, 42
Collette A., 2013, Python and HDF5. O’Reilly, <http://www.h5py.org/>
Correa C. A., Schaye J., Wyithe J. S. B., Duffy A. R., Theuns T., Crain R. A., Bower R. G., 2018, *MNRAS*, **473**, 538
Crain R. A., et al., 2015, *MNRAS*, **450**, 1937
Dalla Vecchia C., Schaye J., 2012, *MNRAS*, **426**, 140
Das S., Mathur S., Gupta A., Nicastro F., Krongold Y., 2019, *ApJ*, **887**, 257
Davies J. J., Crain R. A., Oppenheimer B. D., Schaye J., 2020, *Monthly Notices of the Royal Astronomical Society*, **491**, 4462

- Davis M., Efstathiou G., Frenk C. S., White S. D. M., 1985, *ApJ*, **292**, 371
- Dekel A., Birnboim Y., 2006, *Monthly notices of the royal astronomical society*, **368**, 2
- Dolag K., Borgani S., Murante G., Springel V., 2009, *MNRAS*, **399**, 497
- Faerman Y., Sternberg A., McKee C. F., 2017, *ApJ*, **835**, 52
- Ferland G. J., Korista K. T., Verner D. A., Ferguson J. W., Kingdon J. B., Verner E. M., 1998, *Publications of the Astronomical Society of the Pacific*, **110**, 761
- Ferland G. J., et al., 2013, *Rev. Mex. Astron. Astrofis.*, **49**, 137
- Gatuzz E., Churazov E., 2018, *MNRAS*, **474**, 696
- Gu M. F., Chen H., Brown G. V., Beiersdorfer P., Kahn S. M., 2007, *ApJ*, **670**, 1504
- Gu L., et al., 2019, *A&A*, **627**, A51
- Gupta A., Mathur S., Krongold Y., Nicastro F., Galeazzi M., 2012, *ApJ*, **756**, L8
- Gupta A., Mathur S., Galeazzi M., Krongold Y., 2014, *Ap&SS*, **352**, 775
- Gupta A., Mathur S., Krongold Y., 2017, *ApJ*, **836**, 243
- Haardt F., Madau P., 2001, in Neumann D. M., Tran J. T. V., eds, *Clusters of Galaxies and the High Redshift Universe Observed in X-rays*. ([arXiv:astro-ph/0106018](https://arxiv.org/abs/astro-ph/0106018))
- Hellsten U., Gnedin N. Y., Miralda-Escudé J., 1998a, *ApJ*, **509**, 56
- Hellsten U., Gnedin N. Y., Miralda-Escudé J., 1998b, *ApJ*, **509**, 56
- Hodges-Kluck E. J., Miller M. J., Bregman J. N., 2016, *ApJ*, **822**, 21
- Hummels C. B., et al., 2019, *ApJ*, **882**, 156
- Hunter J. D., 2007, *Computing in Science & Engineering*, **9**, 90
- Johnson S. D., Chen H.-W., Mulchaey J. S., 2015, *MNRAS*, **449**, 3263
- Johnson S. D., Chen H.-W., Mulchaey J. S., Schaye J., Straka L. A., 2017, *ApJ*, **850**, L10
- Johnson S. D., et al., 2019, *ApJ*, **884**, L31
- Jones E., Oliphant T., Peterson P., et al., 2001, *SciPy: Open source scientific tools for Python*, <http://www.scipy.org/>
- Kaastra J., 2018, private communication
- Kereš D., Katz N., Fardal M., Davé R., Weinberg D. H., 2009, *Monthly Notices of the Royal Astronomical Society*, **395**, 160
- Kovács O. E., Bogdán Á., Smith R. a. K., Kraft R. P., Forman W. R., 2019, *ApJ*, **872**, 83
- Kuntz K. D., Snowden S. L., 2000, *ApJ*, **543**, 195
- Lide D. R., ed. 2003, *CRC Handbook of Chemistry and Physics*, 84 edn. CRC Press LLC, Boca Raton
- Lumb D., den Herder J.-W., the Athena Science Team 2017, *Issue/Revision 2.01*, Athena Science Requirements Document. European Space Agency, European Space Research and Technology Centre, Keplerlaan 1, 2201 AZ Noordwijk, The Netherlands
- McAlpine S., et al., 2016, *Astronomy and Computing*, **15**, 72
- McCourt M., Oh S. P., O’Leary R., Madigan A.-M., 2018, *MNRAS*, **473**, 5407
- Meiring J. D., Tripp T. M., Werk J. K., Howk J. C., Jenkins E. B., Prochaska J. X., Lehner N., Sembach K. R., 2013, *ApJ*, **767**, 49
- Miller M. J., Bregman J. N., 2015, *ApJ*, **800**, 14
- Mitchell P. D., Schaye J., Bower R. G., Crain R. A., 2019, *arXiv e-prints*, p. [arXiv:1910.09566](https://arxiv.org/abs/1910.09566)
- Morton D. C., 2003, *The Astrophysical Journal Supplement Series*, **149**, 205
- Mroczkowski T., et al., 2019, *Space Sci. Rev.*, **215**, 17
- Nelson D., et al., 2018, *MNRAS*, **477**, 450
- Nicastro F., et al., 2018, *Nature*, **558**, 406
- Oliphant T. E., 2006, *Guide to NumPy*. Trelgol Publishing, USA
- Oppenheimer B. D., et al., 2016, *MNRAS*, **460**, 2157
- Oppenheimer B. D., Segers M., Schaye J., Richings A. J., Crain R. A., 2018, *MNRAS*, **474**, 4740
- Peeples M. S., et al., 2019, *ApJ*, **873**, 129
- Pérez F., Granger B. E., 2007, *Computing in Science & Engineering*, **9**, 21
- Perna R., Loeb A., 1998, *ApJ*, **503**, L135
- Pillepich A., et al., 2018, *MNRAS*, **473**, 4077
- Planck Collaboration et al., 2014, *A&A*, **571**, A1
- Prochaska J. X., Zheng Y., 2019, *Monthly Notices of the Royal Astronomical Society*, **485**, 648
- Prochaska J. X., Weiner B., Chen H. W., Mulchaey J., Cooksey K., 2011, *ApJ*, **740**, 91
- Rahmati A., Schaye J., Crain R. A., Oppenheimer B. D., Schaller M., Theuns T., 2016, *MNRAS*, **459**, 310
- Ravi V., 2019, *ApJ*, **872**, 88
- Roca-Fàbrega S., et al., 2019, *MNRAS*, **484**, 3625
- Rosas-Guevara Y. M., et al., 2015, *MNRAS*, **454**, 1038
- Schaller M., Dalla Vecchia C., Schaye J., Bower R. G., Theuns T., Crain R. A., Furlong M., McCarthy I. G., 2015, *MNRAS*, **454**, 2277
- Schaye J., et al., 2015, *MNRAS*, **446**, 521
- Smith R. K., et al., 2016, in *Space Telescopes and Instrumentation 2016: Ultraviolet to Gamma Ray*. p. 99054M, doi:10.1117/12.2231778
- Springel V., 2005, *MNRAS*, **364**, 1105
- Springel V., White S. D. M., Tormen G., Kauffmann G., 2001, *MNRAS*, **328**, 726
- Stern J., Fielding D., Faucher-Giguère C.-A., Quataert E., 2019, *MNRAS*, **488**, 2549
- Tepper-García T., Richter P., Schaye J., Booth C. M., Dalla Vecchia C., Theuns T., Wiersma R. P. C., 2011, *MNRAS*, **413**, 190
- Tepper-García T., Richter P., Schaye J., 2013, *MNRAS*, **436**, 2063
- The Lynx Team 2018, *arXiv e-prints*,
- Tripp T. M., Sembach K. R., Bowen D. V., Savage B. D., Jenkins E. B., Lehner N., Richter P., 2008, *ApJS*, **177**, 39
- Tumlinson J., et al., 2011, *Science*, **334**, 948
- Tumlinson J., Peeples M. S., Werk J. K., 2017, *ARA&A*, **55**, 389
- Verner D. A., Verner E. M., Ferland G. J., 1996, *Atomic Data and Nuclear Data Tables*, **64**, 1
- Voit G. M., 2019, *ApJ*, **880**, 139
- Walsh S., McBreen S., Martin-Carrillo A., Dauser T., Wijers N., Wilms J., Schaye J., Barret D., 2020, *Detection capabilities of the Athena X-IFU for the warm-hot intergalactic medium using gamma-ray burst X-ray afterglows*, in prep.
- Wendland H., 1995, *Advances in Computational Mathematics*, **4**, 389
- Werk J. K., et al., 2014, *ApJ*, **792**, 8
- Werk J. K., et al., 2016, *ApJ*, **833**, 54
- Wiersma R. P. C., Schaye J., Smith B. D., 2009a, *MNRAS*, **393**, 99
- Wiersma R. P. C., Schaye J., Theuns T., Dalla Vecchia C., Tornatore L., 2009b, *MNRAS*, **399**, 574
- Wijers N. A., Schaye J., Oppenheimer B. D., Crain R. A., Nicastro F., 2019, *MNRAS*, **488**, 2947
- Wu C., Gao X., 2019, *Scientific Reports*, **9**, 7463
- de Plaa J., Zhuravleva I., Werner N., Kaastra J. S., Churazov E., Smith R. K., Raassen A. J. J., Grange Y. G., 2012, *A&A*, **539**, A34
- den Herder J. W., et al., 2001, *A&A*, **365**, L7
- van de Voort F., Schaye J., Booth C., Haas M. R., Dalla Vecchia C., 2011, *Monthly Notices of the Royal Astronomical Society*, **414**, 2458
- van de Voort F., Springel V., Mandelker N., van den Bosch F. C., Pakmor R., 2019, *MNRAS*, **482**, L85

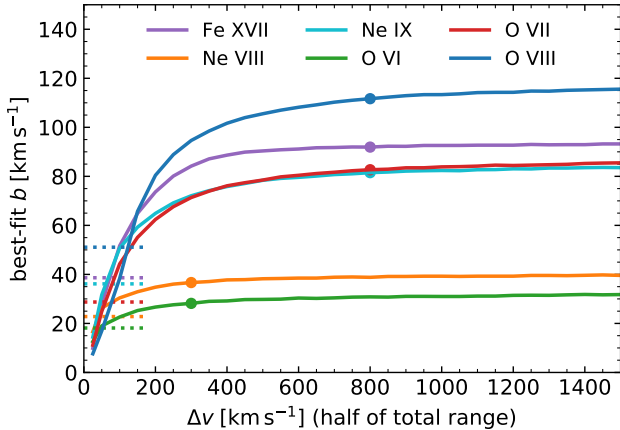


Figure A1. The best-fit b parameter (eqs. 4, 5, and 6) for the different ions’ absorption lines (Table 2, different colors) as a function of the line-of-sight velocity range within which the column density and EW are measured. The indicated velocities are the maximum differences relative to the highest-optical-depth pixel, which is half the full velocity range. The filled points indicate the velocity windows used for each ion in Fig. 3 and throughout the paper, and the dashed lines indicate the thermal broadening for each ion at the temperature where its CIE ionization fraction is largest.

APPENDIX A: MEASURING COLUMN DENSITIES AND EQUIVALENT WIDTHS

In Table 3, we parametrised the relation between column densities and rest-frame equivalent widths measured in a specific velocity range around the maximum-optical-depth position. Here, we explore how the relation depends on the velocity range over which both are measured. We parametrise this relation with the best-fit b parameter (eqs. 4, 5, and 6), assuming a single (or doublet, for O VIII) Voigt profile.

Fig. A1 shows the dependence of the best-fit b parameter on the velocity window used. Since structures and correlations on scales approaching half the box size ($\Delta v \approx 3200 \text{ km s}^{-1}$) cannot be reliably measured in a periodic box, we only show best-fit values up to $\Delta v = 1500 \text{ km s}^{-1}$.

For very small velocity ranges, b parameters are lower than a single absorption component at a typical temperature for high column density absorbers would give. (Low column density absorbers are unsaturated and the fit will therefore not be sensitive to their line widths.) However, the smallest ranges are close to or below the FWHM for such line profiles, so we cannot expect those ranges to be reliable. We interpret the initial rise with velocity range to be due to the velocity window encompassing more absorption from a single absorber or multiple correlated absorbers as the range is increased, and reaching a plateau when all the correlated absorption is included.

For the UV ions (O VI and Ne VIII), this plateau is reached roughly at the velocity cut $\Delta v = \pm 300 \text{ km s}^{-1}$ that we used (filled green and orange points in Fig. A1). This cut was motivated by the observations of Tumlinson et al. (2011) and choices by Johnson et al. (2015) and Burchett

et al. (2019), and is apparently also reasonable for our simulated systems.

For the X-ray ions, we wanted to make sure the velocity range was not too small to probe with the Athena X-IFU, but there was otherwise no clear choice. Based on Fig. A1, we chose a velocity window $\Delta v = \pm 800 \text{ km s}^{-1}$ for these (filled red, blue, purple, and cyan points in Fig. A1). This is large enough to be in the plateau region for these ions, but stays clear of the half box size.

Note that Wijers et al. (2019) found a larger best-fit b parameter for O VIII using the same set of sightlines, but measuring column densities and EWs over the full sightlines. The difference is not due to the inclusion of damping wings in the spectra in this work, which makes very little difference. Instead, it is driven by a subset of high column density sightlines that contain two strong absorbers, resulting from an alignment of two particular high-mass haloes along the Z-axis of the simulation (our line-of-sight direction). This affects best-fit b parameters at Δv approaching half the box size. These haloes also affect the large- Δv best-fit b parameters for Fe XVII and Ne IX.

APPENDIX B: HOW TO SPLIT THE CDDFS

When splitting the CDDFs into contributions from absorption by haloes of different masses, we considered only particles in haloes in each chosen mass range.

For comparison, we also used a method where we attributed a pixel to a halo mass bin by checking whether any central galaxy in the same 6.25 cMpc slice along the line of sight was within R_{200c} (projected) for each absorption system, and if so, which one was closest to that system in normalised impact parameter units of r_{\perp} / R_{200c} . However, low-mass haloes show flat absorption profiles and, depending on the ion in question, have virial temperatures well below the temperatures where that ion exists in CIE. Some of the absorption attributed to low-mass haloes in this mask-split method will therefore actually be due to higher-mass haloes nearby.

We show a comparison of which absorption is attributed to which halo using the halo-gas-only projections and the map-split method in Fig. B1, for O VIII. The top left panel is the same as Fig. 5, but using the mask-split method. We see that the modal column density increases with halo mass up to the ‘break’ in the CDDF, after which modal column densities decrease again and distributions become flatter.

In the top, middle panel (‘all halo gas’), the grey line shows absorption from haloes at any mass, while the brown lines show CDDFs from all-gas (dashed) and halo-only (solid) column density maps, with only the contributions from pixels within R_{200c} of an $M_{200c} > 10^9 M_{\odot}$ halo. The differences between these three methods of measuring how much absorption is due to haloes are relatively small at high column densities, especially between the solid and dashed brown lines, which represent the two main ways to define the CDDF coming from roughly within the virial radii of haloes. This means that the split between halo and extra-halo absorption is relatively robust. (Note that gas outside R_{200c} or other virial radius definitions may still be associated with haloes, so where exactly the line between CGM and IGM lies is not generally agreed on.)

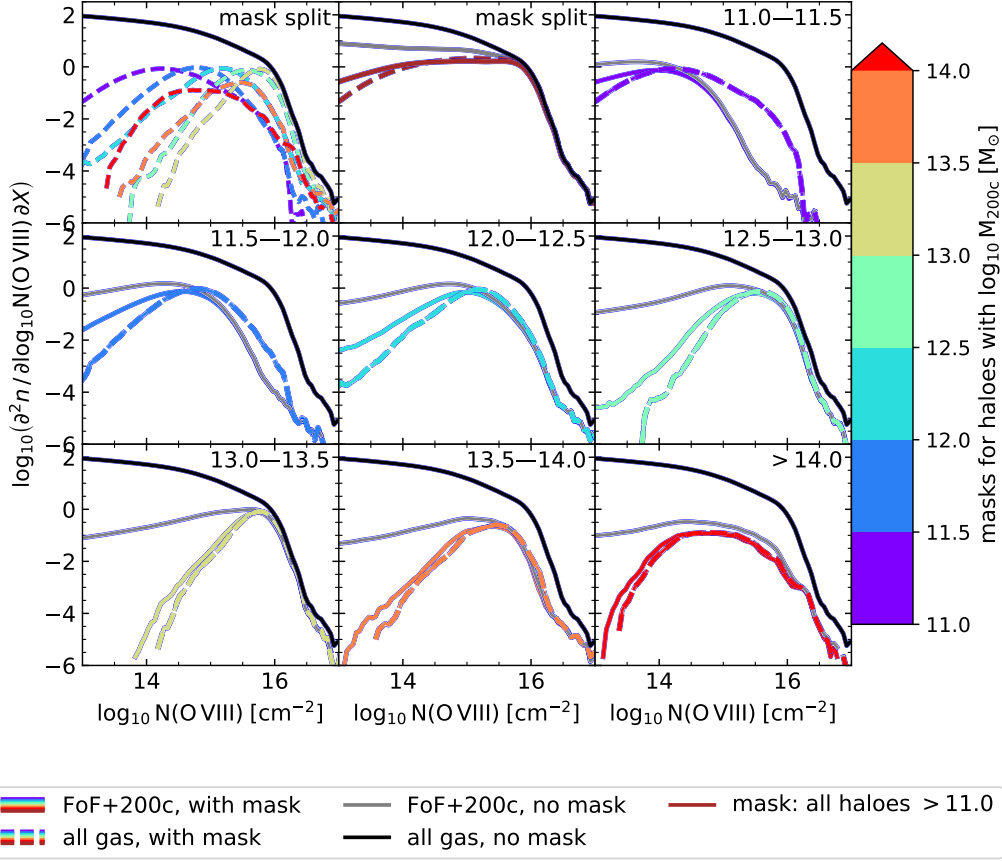


Figure B1. A comparison between the column density distribution arising from haloes in different mass ranges by two methods. In the first, the CDDF is constructed in the same way as from all gas, but only considering absorption from gas within haloes in each mass range. By within haloes, we mean FoF particles and anything within R_{200c} of the centre of potential of each halo. For the second method, the column density distribution attributed to a halo mass bin is determined by, for each pixel in the column density map, checking which halo, if any, matches the line-of-sight slice of the absorber, is within R_{200c} , and is closest in units of r_{\perp}/R_{200c} (mask-split). This plot shows the distributions for O VIII. The black lines show the total CDDF in all panels. In the top left panel, dashed coloured lines show the part of the total CDDF attributed to the halo mass range corresponding to that colour (colour bar) using the mask-split method. The ‘all halo gas’ panel uses masks for all haloes $M_{200c} > 10^{11} M_{\odot}$, cutting out parts attributed to haloes with $10^9 M_{\odot} < M_{200c} < 10^{11} M_{\odot}$. The masks are applied to an absorption map including only gas in haloes (of any mass, including $< 10^9 M_{\odot}$). The brown lines in this panel come from combining the masks for all the haloes with $M_{200c} \geq 10^{11} M_{\odot}$. In the rest of the panels, the range in the top left corner indicates the range of halo masses ($\log_{10} M_{200c}/M_{\odot}$) for which the gas is included in the column density maps the CDDFs are derived from. The dashed line of the colour matching the mass range shows the contribution according to the mask-split method applied to the column density maps for all gas, and the coloured solid lines show CDDFs from only the gas in the indicated range attributed to the same halo mass range by the mask-split method. The grey lines in the panels for specific halo masses show the halo-gas-only CDDFs used in the main text (Fig. 5).

In the panels for specific halo masses, we can similarly compare the dashed and solid lines of the colour matching the halo mass in the panel to the grey line to get a sense of how robust the map-split and FoF-only methods are for determining which absorption comes from haloes. The agreement between these methods clearly depends on the halo mass. The higher column density absorption projected within R_{200c} of the lowest-mass haloes is clearly mostly due to gas outside those haloes, showing that much of the absorption attributed to these haloes using the mask-split method

is simply due to these haloes being in roughly the same place as whatever structure is causing the absorption.

As the halo mass increases, the different methods agree well at column densities at or above the modal column density for that mass. The difference between the grey and coloured solid lines shows that this is largely due to lower-column-density absorption from gas in the FoF groups of haloes that is outside R_{200c} in projection. This will be due, in part, to the FoF groups not agreeing exactly with the overdensity definition of haloes, but also because SPH particles centred inside R_{200c} may extend beyond that radius.

The very low column densities likely result, at least in part, from ‘edge effects’, where a particular sightline probes (the edge of) one or very few SPH particles at the outer extent of the FoF group.

Differences between the solid and dashed lines show absorption attributed to haloes (i.e. within R_{200c} in the plane of the sky), but not due to gas within the FoF group. This tends to lead to slightly more high-column-density absorbers, but the larger effect is typically at lower column densities, where gas outside the FoF groups is more important (Fig. 6).

For the other ions, the picture is very similar, except that the mass above which the methods agree at high column densities changes: the largest mass bin with disagreements at most about as bad as $M_{200c} = 10^{11.5} - 10^{12} M_{\odot}$ for O VIII is:

- $M_{200c} = 10^{10.5} - 10^{11} M_{\odot}$ for O VI (not shown here),
- $M_{200c} = 10^{11} - 10^{11.5} M_{\odot}$ for Ne VIII and O VII, and
- $M_{200c} = 10^{11.5} - 10^{12} M_{\odot}$ for Ne IX, Fe XVII (and O VIII).

Above those ranges, we consider the contributions of these ions to the CDDF to be fairly robust. The limiting mass for reliability increases with the CIE temperature range of the ions.

In summary the attribution of absorption to haloes shown in Fig. 5 is fairly robust for higher-mass haloes ($> 10^{12} M_{\odot}$, and lower for some ions), for column densities above the peak of the CDDF for each M_{200c} bin. However, at lower column densities, the CDDF for a set of haloes depends quite strongly on how absorption and haloes are connected. The fraction of absorption beyond the CDDF breaks due to haloes does depend on these choices somewhat, but they do not change the qualitative conclusions.

APPENDIX C: REDSHIFT EVOLUTION

In Fig. C1, we investigate the redshift evolution of halo radial profiles. This is relevant for all the ions discussed in this work, but we focus on O VII and O VIII, which should be the most easily observed X-ray lines in this sample, and Ne VIII, which was observed at $z > 0.48$, but is not observable at $z = 0.1$ (Burchett et al. 2019). We compare column densities measured through the same comoving slice thickness (6.25 cMpc) at both redshifts.

The median changes are generally small ($\lesssim 0.2$ dex) at the halo masses where the column densities are largest, and within the range of the 80 per cent scatter. The redshift evolution is larger at larger and smaller halo masses, however. The changes are in line with how T_{200c} evolves: at the same M_{200c} , T_{200c} is somewhat larger at $z = 0.5$ than $z = 0.1$. Note that for a fixed density profile, M_{200c} and R_{200c} at the two redshifts will also differ. The differences do mean that any comparisons of absorbers to data should be done at matching redshifts.

Fig. C2, we similarly consider the evolution of the CDDFs of these ions from redshift 0.1 to 0.5. We see the CDDFs change in ways consistent with the radial profiles: the distributions look similar, but at $z = 0.5$, they look like those for somewhat higher-mass $z = 0.1$ haloes. Another difference is in the total gas CDDF. All haloes together contribute less to the high-column-density absorption at $z = 0.5$

than at $z = 0.1$. This might be related to how the FoF groups are defined: by particle separation relative to the average, which means that haloes will be ‘cut off’ at higher densities at the higher redshift. Overall evolution of the EAGLE O VII and O VIII CDDFs was discussed in more detail by Wijers et al. (2019), and Rahmati et al. (2016) discussed the Ne VIII CDDF evolution, as well as that of O VI.

Note that the highest mass bin only has 5 haloes at $z = 0.5$, and 9 at $z = 0.1$, so some changes here might be explained by selection effects (lower typical masses at higher redshift) and small sample sizes.

This paper has been typeset from a \LaTeX file prepared by the author.

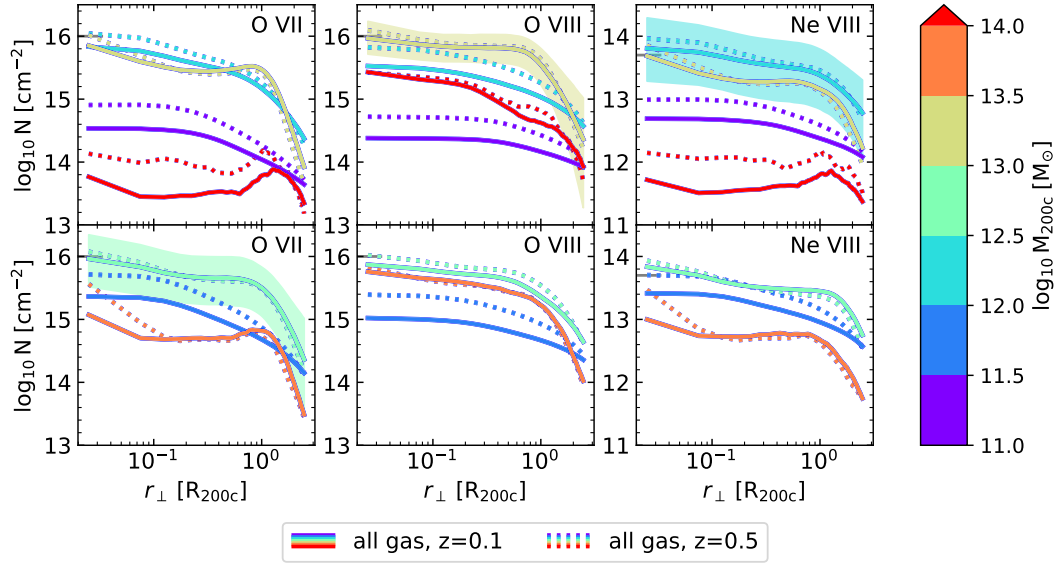


Figure C1. A comparison of the radial profiles for O VII, O VIII, and Ne VIII between redshifts 0.1, as used throughout this work, and $z = 0.5$. The mass bins are split over top and bottom panels for legibility. We see that at halo masses where the column densities peak, the median column density is similar at the two redshifts, but the peak range may be larger at $z = 0.5$, and the profiles at higher and lower halo masses change more. The central 80 per cent scatter is shown for the peak halo mass at $z = 0.1$ with the shaded bands.

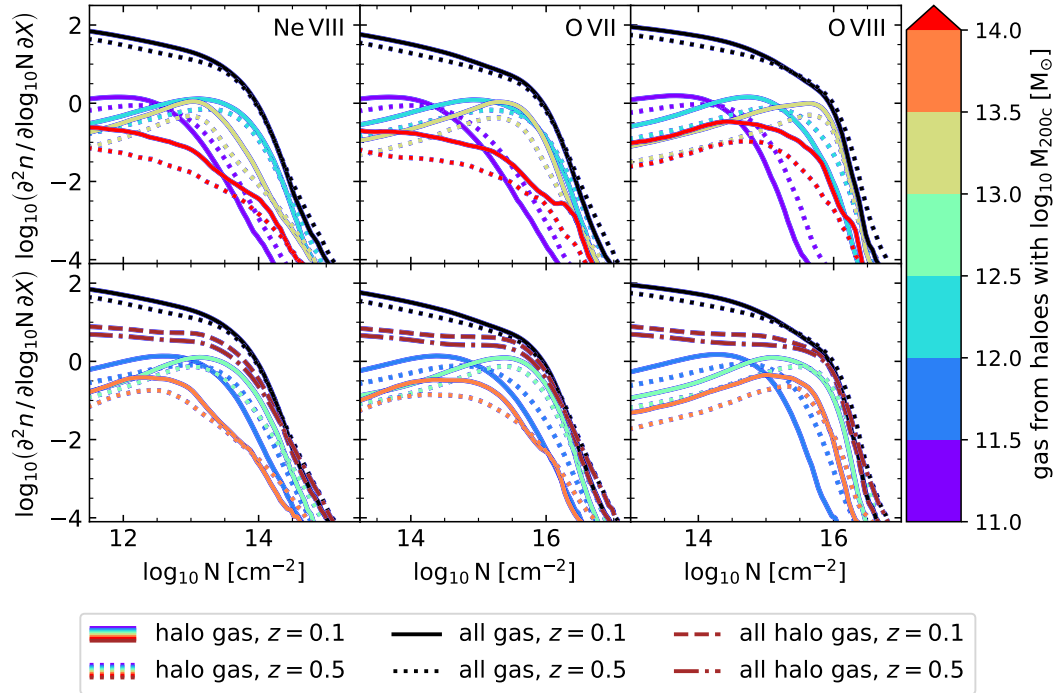


Figure C2. A comparison between the column density distributions of Ne VIII, O VII, and O VIII at $z = 0.1$ (solid and dashed lines) and $z = 0.5$ (dotted and dash-dotted lines). The CDFs for different halo mass ranges are derived from column density maps using only gas in FoF groups of haloes of the different masses. The colours match those of Fig. 5, but the lines for different halo masses are split over top and bottom panels for legibility.